

Trans-dimensional Bayesian joint inversion of magnetotelluric and geomagnetic depth sounding responses to constrain mantle electrical discontinuities

Hongbo Yao,^{1,2} Zhengyong Ren³,^{1,2,3} Jingtian Tang,^{1,3} Rongwen Guo^{1,3} and Jiayong Yan^{2,4}

¹Key Laboratory of Metallogenic Prediction of Nonferrous Metals and Geological Environment Monitoring Ministry of Education, School of Geosciences and Info-Physics, Central South University, Changsha 410083, China. E-mail: renzhengyong@csu.edu.cn

²SinoProbe Laboratory, Ministry of Natural Resources, Beijing 100094, China

³Hunan Key Laboratory of Nonferrous Resources and Geological Disaster Exploration, Changsha 410083, China

⁴Chinese Academy of Geological Sciences, Beijing 100037, China

Accepted 2023 January 20. Received 2022 December 24; in original form 2022 August 18

SUMMARY

Joint inversion of magnetotelluric (MT) and geomagnetic depth sounding (GDS) responses can constrain the crustal and mantle conductivity structures. Previous studies typically use either deterministic inversion algorithms that provide limited information on model uncertainties or using stochastic inversion algorithms with a predetermined number of layers that is generally not known *a priori*. Here, we present a new open-source Bayesian framework for the joint inversion of MT and GDS responses to probe 1D layered Earth's conductivity structures. Within this framework, model uncertainties can be accurately estimated by generating numerous models that fit the observed data. A trans-dimensional Markov Chain Monte Carlo (MCMC) method is employed to self-parametrize the model parameters, where the number of layers is treated as an inversion parameter that is determined automatically by the data. This adaptability can overcome the under or over-parametrization problem and may be able to automatically detect the conductivity discontinuities in the Earth's interior. To accelerate the computations, a large number of Markov chains with different initial states can be run simultaneously using the MPI parallel technique. Synthetic data sets are used to validate the feasibility of our method and illustrate how separate and joint inversions, as well as various priors affect the posterior model distributions. The trans-dimensional MCMC algorithm is then applied to jointly invert the MT and GDS responses estimated at the Tucson geomagnetic observatory, North America. Our results not only contain model uncertainty estimates but also indicate two distinct conductivity discontinuities at around 85 and 440 km, which are likely related to the lithosphere-asthenosphere boundary and the upper interface of the mantle transition zone, respectively.

Key words: Electrical properties; Geomagnetic induction; Magnetotellurics; Joint inversion; Probability distributions; Statistical methods.

1 INTRODUCTION

Electrical conductivity is sensitive to temperature variations, water content and the presence of melt (Yoshino & Katsura 2013). Imaging the electrical conductivity structure of the Earth's interior is crucial to understand the composition, structures and dynamics of the Earth's interior. Two kinds of natural source electromagnetic (EM) sounding techniques, which are magnetotelluric (MT) and geomagnetic depth sounding (GDS), have been used for imaging deep conductivity structures. The MT method employs plane wave EM variations with periods shorter than several hours to image the conductivity structures from the crust down to the upper mantle (Chave & Jones 2012). The GDS method exploits two kinds of geomagnetic variations. One is the diurnal geomagnetic variations mostly during the solar quiet (Sq) phase (Zhang *et al.* 2022). Its periods are from 4 h to 1 d and mainly originate from the mid-latitude ionospheric current system. Using these data, we can probe the conductivity structures of the upper mantle and transition zone (Guzavina *et al.* 2019; Zhang *et al.* 2022). The other are the geomagnetic variations between several days and several months originating from the magnetospheric ring current, constraining conductivity

distribution from the transition zone to the lower mantle (Munch *et al.* 2018; Yuan *et al.* 2020; Zhang *et al.* 2020). This study aims to jointly invert the MT and GDS responses, which can constrain both the crustal and mantle conductivity structures with improved resolution and reduced uncertainty.

There were several studies on the joint inversion of MT and GDS responses (Egbert & Booker 1992; Bahr *et al.* 1993; Schultz *et al.* 1993; Lizarralde *et al.* 1995; Ichiki *et al.* 2001; Utada *et al.* 2003; Shimizu *et al.* 2010; Chen *et al.* 2022). Most previous studies formulated the joint inversion problem as a regularized least square problem and solved it in terms of gradient-based optimization methods. These results relied on initial models and were easy to fall into local minima. In addition, they hardly provided a quantitative assessment of model uncertainty, which is crucial for reliable interpretation (Ren & Kalscheuer 2020).

The Bayesian Markov Chain Monte Carlo (MCMC) algorithm can provide quantitative estimates of model uncertainty by exploring a large number of model candidates. The standard fixed-dimensional MCMC algorithm, which uses a fixed number of layers during inversion, was used to invert MT (Grandis *et al.* 1999; Guo *et al.* 2014) and GDS responses (Khan *et al.* 2006, 2011; Civet *et al.* 2015; Püthe *et al.* 2015a; Verhoeven *et al.* 2021). It was combined with the stochastic Covariance Matrix Adaptation Evolution Strategy optimization algorithm (Grayver & Kuvshinov 2016) to estimate the model uncertainty in the joint inversion of ionospheric and magnetospheric GDS responses (Munch *et al.* 2020), satellite tidal and magnetospheric GDS responses (Grayver *et al.* 2017; Kuvshinov *et al.* 2021), as well as MT and GDS responses (Chen *et al.* 2022). However, in inversion, the number of layers was generally not known *a priori*, the fixed-dimensional MCMC algorithm may lead to under or over parametrization problem and parametrization dependent model uncertainty.

In contrast, the trans-dimensional Bayesian algorithm (Green 1995) treats the number of layers as an unknown inversion parameter and tries to determine its value during the inversion. The trans-dimensional Bayesian algorithm has two merits. First, it can self-parametrize the model parameters and thus avoid the under or over parametrization problem. This flexibility may have the potential to automatically detect the interfaces of conductivity jumps, which are important for understanding the material exchange in the deep Earth. Secondly, it has a parsimony property (Malinverno 2002), which is models with few layers have high probabilities to be accepted, thus the algorithm is computationally efficient. The trans-dimensional Bayesian algorithm has been widely used in various geophysical inverse problems, such as seismic imaging (Bodin & Sambridge 2009; Bodin *et al.* 2012), direct resistivity inversion (Malinverno 2002), controlled source EM inversion (Ray & Key 2012; Gehrmann *et al.* 2015), airborne EM inversion (Minsley 2011; Yin *et al.* 2014; Blatter *et al.* 2018; Minsley *et al.* 2021), and MT inversion (Mandolesi *et al.* 2018; Xiang *et al.* 2018; Guo *et al.* 2019; Seillé & Visser 2020; Peng *et al.* 2022). They were also used in the joint inversion of MT and CSEM data sets (Blatter *et al.* 2019) as well as direct current resistivity and transient electromagnetic data sets (Peng *et al.* 2021). But, to the best of our knowledge, there is no trans-dimensional MCMC study on jointly inverting MT and GDS data sets. One thing to note here is that the MCMC algorithm is now only workable in 1D problem setups. For 3D setups, the MCMC algorithm is impracticable due to enormous computational costs.

In this study, utilizing the trans-dimensional Bayesian MCMC method, we present a new open-source framework and tool to jointly invert MT and GDS data sets. First, various MT and GDS transfer functions (TFs) are considered so that we can deal with ground and satellite geomagnetic data, as well as ionospheric and magnetospheric sources. The 1D layered structure is adopted as the inversion model where both the number of layers and layer conductivities are treated as unknowns. Then, the trans-dimensional MCMC sampling algorithm is used to generate posterior model distribution, which provides model uncertainties. The message passing interface (MPI) parallelization technique is used to accelerate the computations so that a large number of Markov chains with different initial states can run simultaneously. Finally, we apply this framework to both synthetic and real field data.

2 JOINT INVERSION FRAMEWORK

2.1 Transfer functions

The MT source can be approximated as the vertically incident plane wave. Using the orthogonal EM fields measured at the surface or sea bottom, we can estimate the scalar MT impedance, which relates the horizontal electric field with the horizontal magnetic field by (Chave & Jones 2012)

$$Z_{MT}(\mathbf{r}_a, \omega) = \frac{E_x(\mathbf{r}_a, \omega)}{H_y(\mathbf{r}_a, \omega)} = -\frac{E_y(\mathbf{r}_a, \omega)}{H_x(\mathbf{r}_a, \omega)}, \quad (1)$$

where $Z_{MT}(\mathbf{r}_a, \omega)$ denotes the scalar MT impedance at location \mathbf{r}_a for an angular frequency of ω and the subscripts x and y denote the northward and eastward directions.

The commonly used MT responses are the apparent resistivity $\rho_a(\mathbf{r}_a, \omega)$ and phase $\phi(\mathbf{r}_a, \omega)$, which are obtained from impedance by

$$\rho_a(\mathbf{r}_a, \omega) = \frac{1}{\omega \mu_0} |Z_{MT}(\mathbf{r}_a, \omega)|^2, \quad (2)$$

$$\phi(\mathbf{r}_a, \omega) = \tan^{-1} \left[\frac{\text{Im}(Z_{MT}(\mathbf{r}_a, \omega))}{\text{Re}(Z_{MT}(\mathbf{r}_a, \omega))} \right], \quad (3)$$

where μ_0 is the magnetic permeability of free space and Re and Im denote the real and imaginary parts of the impedance.

The GDS method relies mainly on the geomagnetic fields measured by ground geomagnetic observatories or/and satellites. These geomagnetic field variations originate from the global ionospheric and magnetospheric sources (Kuvshinov 2008). Due to the different source

Table 1. List of GDS TFs supported by our inversion framework for different geomagnetic data types and different sources. The detailed descriptions of these TFs are discussed in the main text.

Transfer functions	Data type	Main source
global Q -response	ground/satellite	magnetospheric ring current
global C -response	ground/satellite	magnetospheric ring current
local C -response	ground	magnetospheric ring current
global-to-local TFs	ground	ionospheric Sq current/magnetospheric ring current

morphologies and different data types, various GDS TFs exist. Here, we summarize the GDS TFs supported by our inversion framework and their application scenarios.

2.1.1 Global TFs

From the geomagnetic data measured by a global network of geomagnetic observatories or/and satellites and assuming a 1D layered Earth model, we can estimate the frequency domain global Q -response, which is defined as (Olsen 1999)

$$Q_n(\omega) = \frac{\iota_n^m(\omega)}{\epsilon_n^m(\omega)}, \quad (4)$$

where ϵ_n^m is the spherical harmonic (SH) coefficient of degree n and order m describing the external sources and ι_n^m is the internal SH coefficient induced in the Earth by external sources through EM induction process. The global Q -response can be transformed to the global C -response (Olsen 1999) by

$$C_n(\omega) = \frac{a}{n+1} \frac{1 - \frac{n+1}{n} Q_n(\omega)}{1 + Q_n(\omega)}, \quad (5)$$

where $a = 6371$ km is the Earth's mean radius.

These global responses work for geomagnetic observatory data of both magnetospheric and ionospheric origins. For satellite data, only responses of magnetospheric origin can be estimated since the ionospheric Sq current is purely internal relative to satellite measurements. With observed (i.e. estimated from the data) global responses and an appropriate inversion algorithm, we can probe the globally averaged mantle conductivity structures, which can be used to constrain the mean physicochemical state of the mantle.

2.1.2 Local C -response

To constrain the local conductivity structures beneath a single geomagnetic observatory, local TFs are required. As discussed in Introduction, the geomagnetic variations from several days to several months are dominated by the magnetospheric ring current. As seen at the ground, this current is usually approximated by the first zonal SH Y_1^0 in geomagnetic coordinates. In this case, the local C -response is defined as (Banks 1969)

$$C(\mathbf{r}_a, \omega) = -\frac{a \tan \theta_d}{2} \frac{B_r(\mathbf{r}_a, \omega)}{B_{\theta_d}(\mathbf{r}_a, \omega)}, \quad (6)$$

where $\mathbf{r}_a = (a, \theta, \phi)$ is the location of a given geomagnetic observatory at Earth's surface, θ_d is the geomagnetic colatitude, B_r is the radial component of the magnetic field and B_{θ_d} is the geomagnetic south component of the magnetic field.

For the ionospheric Sq current, which has a much more complex spatial structure, a variant of local C -response was employed (Bahr *et al.* 1993). However, it relies on the assumption that the Sq source can be well approximated by a single SH specific for each period, which is too simplistic (Schmucker 1999; Guzavina *et al.* 2019). Therefore, we will not use the local C -response concept for Sq variations.

2.1.3 Global-to-local TFs

There is increasing evidence that the magnetospheric spatial structure is more complex. To handle complex magnetospheric source structure, Pütthe *et al.* (2015b) proposed new TFs that relate an array of SH coefficients ϵ_n^m describing the global source with the local vertical magnetic field

$$Z(\mathbf{r}_a, \omega) = \sum_{n,m} \epsilon_n^m(\omega) T_n^m(\mathbf{r}_a, \omega), \quad (7)$$

where the double sum specifies a subset of SH for each frequency, $Z(\mathbf{r}_a, \omega)$ is the local vertical magnetic field measured by a single geomagnetic observatory and $T_n^m(\mathbf{r}_a, \omega)$ are the array of TFs called the global-to-local (G2L) TFs (Pütthe *et al.* 2015b). These new TFs can be also applied to Sq variations. Recently, Guzavina *et al.* (2019) implemented the G2L TFs concept to analyse Sq variations. Note that for the ionospheric Sq current, the dominating term is T_{p+1}^p for a period of $T = 24/p$ ($p = 1, 2, \dots, 6$) h. In this study, only dominating terms are used in the inversion.

The various GDS TFs supported by our Bayesian inversion framework are summarized in Table 1. As the input for the joint inversion, these GDS TFs can be arbitrarily combined with the MT apparent resistivity and phase.

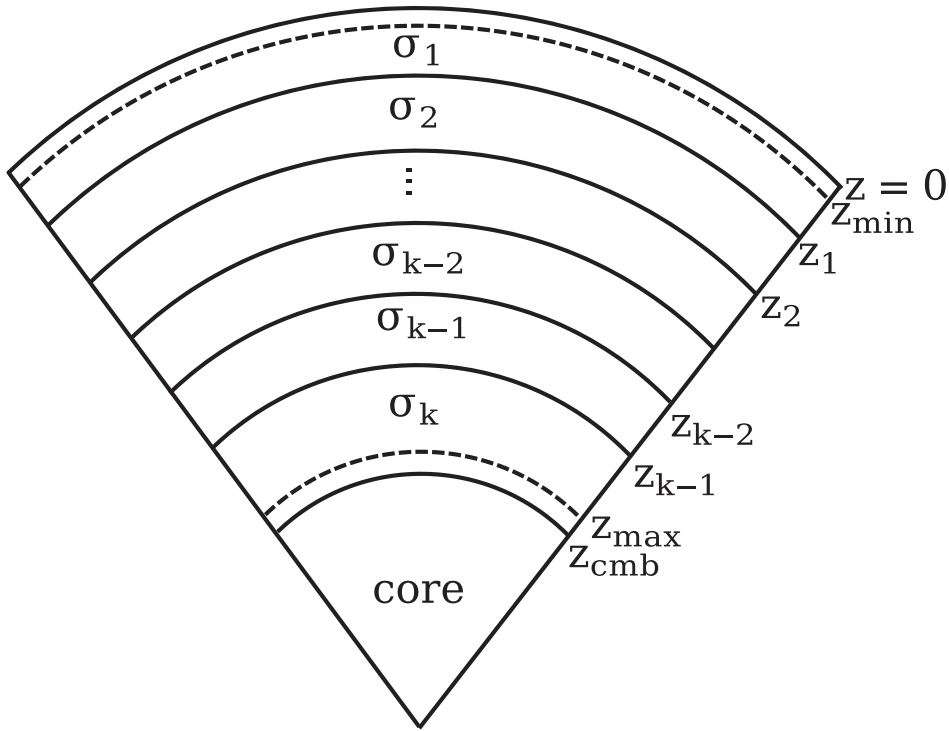


Figure 1. 1D model parametrization of the Earth for the trans-dimensional Bayesian inversion. The inversion domain from the Earth's surface to the core-mantle boundary ($z_{\text{cmb}} = 2890$ km) consists of k layers separated by $k - 1$ layer interfaces. The conductivity of the Earth's core is set to a fixed value of 5×10^5 S/m. The detailed descriptions of the model parametrization are discussed in the main text.

2.2 Model parametrization and forward modelling

We adopt the 1D layered parametrization of the Earth (Fig. 1). The trans-dimensional Bayesian method treats the number of layers, layer interface depths (or layer thicknesses) and layer conductivities as inversion parameters, therefore providing great flexibility for model parametrization. The inversion model parameters \mathbf{m} are defined as

$$\mathbf{m} = [k, \mathbf{z}, \boldsymbol{\sigma}], \quad (8)$$

where k is the number of layers, $\mathbf{z} = [z_1, z_2, \dots, z_{k-1}]$ is the vector of layer interface depths and $\boldsymbol{\sigma} = [\sigma_1, \sigma_2, \dots, \sigma_k]$ denotes the vector of \log_{10} layer conductivities. The number of layers, interface depths and layer conductivities are restricted to fall between the user-given minimum and maximum values, k_{\min} and k_{\max} , z_{\min} and z_{\max} and σ_{\min} and σ_{\max} . Note that we use log-conductivity parametrization to ensure the positivity of conductivity values and to better consider the different orders of magnitude of conductivities. For sampling the interface depths, we use linear parametrization in this study to avoid over-sampling at near-surface depths, where long-period MT and GDS responses lack enough resolution.

We also adopt a constraint to avoid generating extremely thin layers, unless otherwise stated, the minimum allowable layer thickness is taken as (Minsley 2011)

$$h_{\min} = \frac{z_{\max} - z_{\min}}{2k_{\max}}. \quad (9)$$

Unlike the conventional deterministic inversion methods, the gradient information is not needed by the Bayesian method. Therefore, only computation of predicted responses is required during Bayesian inversion. The MT responses for a given layered structure can be computed using the analytic solutions (Ward & Hohmann 1987). For the computations of various GDS responses, we use the recursive formulas described in the appendix of Kuvshinov & Semenov (2012).

2.3 Trans-dimensional Bayesian joint inversion

In the Bayesian framework, the solution to an inverse problem is the posterior probability distribution of the model parameters \mathbf{m} given the observed data \mathbf{d} is known. According to Bayes' theorem, the posterior probability distribution $p(\mathbf{m}|\mathbf{d})$ is given by

$$p(\mathbf{m}|\mathbf{d}) \propto p(\mathbf{d}|\mathbf{m})p(\mathbf{m}), \quad (10)$$

where $p(\mathbf{m})$ is an assumed prior probability distribution and $p(\mathbf{d}|\mathbf{m})$ denotes the likelihood function, which is a measure of data fit. Following the common practices for MT inversion (Egbert *et al.* 1992; Chave & Jones 2012) and GDS inversion (Kelbert *et al.* 2008; Semenov & Kuvshinov 2012; Guzavina *et al.* 2019), we assume the data errors obey a Gaussian distribution with zero mean

$$p(\mathbf{d}|\mathbf{m}) = \sum_{j=1}^M \frac{1}{\sqrt{(2\pi)^{N_j} |\mathbf{C}_{dj}|}} \exp \left\{ -\frac{[\mathbf{d}_j - \mathbf{F}_j(\mathbf{m})]^T \mathbf{C}_{dj}^{-1} [\mathbf{d}_j - \mathbf{F}_j(\mathbf{m})]}{2} \right\}, \quad (11)$$

where M is the number of data types with j denoting the j -th data type (which can be either the MT apparent resistivity and phase or the different GDS TFs), N_j is the number of observed data, \mathbf{d}_j is a vector of observed data, $\mathbf{F}_j(\mathbf{m})$ denotes the forward operator used to compute the predicted responses and \mathbf{C}_{dj} is the data covariance matrix for the j -th data type. Here, we follow the common practices and assume the data errors are normally distributed and uncorrelated. Therefore, \mathbf{C}_{dj} is diagonal with elements being the variances of data errors. Correlated noise may be expected in field data application but a detailed discussion on this topic is beyond the scope of this study. For more discussions on the correlated noise, we refer to Guo *et al.* (2019) and Peng *et al.* (2021).

We assume that the prior knowledge of the interface depths \mathbf{z} and the layer conductivities $\boldsymbol{\sigma}$ are independent (Malinverno 2002), the prior distribution $p(\mathbf{m})$ can be written as

$$p(\mathbf{m}) = p(k)p(\mathbf{z}|k)p(\boldsymbol{\sigma}|k). \quad (12)$$

The number of layers k is restricted to vary between the minimum and maximum allowed number of layers k_{\min} and k_{\max} by a uniform distribution

$$p(k) = \frac{1}{k_{\max} - k_{\min} + 1} = \frac{1}{\Delta k}. \quad (13)$$

The prior distribution for the interface depths is given by

$$p(\mathbf{z}|k) = \frac{(k-1)!}{(\Delta z)^{k-1}}, \quad (14)$$

where $\Delta z = z_{\max} - z_{\min}$ is the depth interval where each layer interface can be located and $(k-1)!$ is the number of ways that $k-1$ layer interfaces can be ordered.

For the layer log-conductivities, several different prior distributions were used in the EM inversion. For example, Blatter *et al.* (2018) used a uniform prior distribution for layer conductivities in Bayesian inversion of airborne EM data. Minsley (2011) compared two multivariate normal distributions for layer conductivities in airborne EM inversion. The first one constrains the layer conductivities to a reference conductivity model, the second one constrains the vertical smoothness of layer conductivities. In this study, we will investigate the uniform and smooth prior distributions for layer conductivities for the joint inversion of MT and GDS responses.

If the prior knowledge only gives the minimum and maximum log-conductivities, the uniform prior distribution of layer conductivities is

$$p(\boldsymbol{\sigma}|k) = \frac{1}{(\sigma_{\max} - \sigma_{\min})^k} = \frac{1}{(\Delta \sigma)^k}. \quad (15)$$

To generate geologically meaningful smooth models, which only contain features that are required by the data (Constable *et al.* 1987), we also consider another multivariate normal distribution adapted from Minsley (2011) to constrain the vertical smoothness of models

$$p(\boldsymbol{\sigma}|k) = \frac{1}{\sqrt{(2\pi)^{k-1} |\mathbf{C}_{\sigma}|}} \exp \left[-\frac{(\nabla \boldsymbol{\sigma})^T \mathbf{C}_{\sigma}^{-1} (\nabla \boldsymbol{\sigma})}{2} \right], \quad (16)$$

where \mathbf{C}_{σ} is the diagonal prior covariance matrix, which controls the smoothness of conductivity models, the conductivity difference at the i -th ($i = 1, 2, \dots, k-1$) interface is $\nabla^i \boldsymbol{\sigma} = \sigma_{i+1} - \sigma_i$. Compared to the original definition of $\nabla^i \boldsymbol{\sigma} = \frac{\sigma_{i+1} - \sigma_i}{h_i - h_{\min}}$ of Minsley (2011), we drop the denominator since using the conductivity difference directly is more intuitive for choosing the prior covariance. In our case, the element of \mathbf{C}_{σ} is exactly the standard deviations of conductivity differences between adjacent layers.

The goal of Bayesian inversion is to estimate the posterior model distribution by sampling the model space. Here, we employ the so-called trans-dimensional or reversible jump MCMC sampling algorithm (Green 1995), which is based on the classical Metropolis-Hastings method (Metropolis *et al.* 1953; Hastings 1970). The trans-dimensional sampling algorithm consists of two steps. First, a candidate model \mathbf{m}' is proposed by perturbing the current model \mathbf{m} according to the proposal distribution $q(\mathbf{m}'|\mathbf{m})$, which will be discussed later. Secondly, the candidate model is either accepted or rejected based on the acceptance probability $\alpha(\mathbf{m}'|\mathbf{m})$

$$\alpha(\mathbf{m}'|\mathbf{m}) = \min \left[1, \frac{p(\mathbf{d}|\mathbf{m}') p(\mathbf{m}') q(\mathbf{m}|\mathbf{m}') |\mathbf{J}|}{p(\mathbf{d}|\mathbf{m}) p(\mathbf{m}) q(\mathbf{m}'|\mathbf{m})} \right], \quad (17)$$

where $|\mathbf{J}|$ denotes the Jacobian of the jump from \mathbf{m} to \mathbf{m}' . To generate the proposal model, we apply the birth-death scheme (Geyer & Møller 1994), where the number of layers of \mathbf{m}' will increase by one, decrease by one or keep unchanged. In this case, $|\mathbf{J}|$ equals unity (Agostinetti & Malinverno 2010) and will be dropped in this study. After computing the acceptance probability of the candidate model, as will be discussed

below, a random number r between 0 and 1 is generated, if $r < \alpha$, the candidate model \mathbf{m}' is accepted as the new model, otherwise the candidate model is rejected and the old model \mathbf{m} is duplicated.

Since the trans-dimensional MCMC approach has not been applied to the joint inversion of MT and GDS responses, we give here the outline of our algorithm and the specific details relevant to each step. These details would be beneficial for readers to understand our computer code implementation.

2.3.1 Initialization

The inversion is initialized with a two-layered conductivity model ($k_{\min} = 2$), the interface depth is randomly generated within $[z_{\min}, z_{\max}]$ and the log-conductivities of both layers are generated randomly within $[\sigma_{\min}, \sigma_{\max}]$.

2.3.2 Proposal distributions

After initializing the Markov chain, we modify the last model of the chain with one of the following perturbations to generate the candidate model, each perturbation is performed with a probability of p .

(1) Birth ($p = 1/4$): A new layer interface is added at a random depth between z_{\min} and z_{\max} . Randomly select the upper or lower layer of the interface, the layer conductivity is perturbed by a Gaussian distribution with the current conductivity as its mean. $k' = k + 1$.

(2) Death ($p = 1/4$): Randomly select a layer interface to delete and merge the two layers separated by the interface into a new layer. The conductivity of the new layer is set to be the conductivity of either the upper or lower layer of the deleted interface. $k' = k - 1$.

(3) Move ($p = 1/4$): Randomly select a layer interface, its depth is perturbed by a Gaussian distribution with the current depth as its mean. $k' = k$.

(4) Update ($p = 1/4$): Randomly select a layer, its conductivity is perturbed by a Gaussian distribution with the current conductivity as its mean. $k' = k$.

Note that if the generated candidate model violates the prior information or the layer thickness is thinner than h_{\min} , this model will be rejected.

The proposal distribution $q(\mathbf{m}'|\mathbf{m})$ can be written as

$$q(\mathbf{m}'|\mathbf{m}) = q(k'|k)q(\mathbf{z}'|k', \mathbf{z})q(\boldsymbol{\sigma}'|k', \boldsymbol{\sigma}). \quad (18)$$

According to the above perturbations, the proposal distribution for the number of layers, layer interface depths and layer conductivities are respectively

$$q(k'|k) = \begin{cases} 1/4 & \text{birth} \\ 1/4 & \text{death} \\ 1/4 & \text{move} \\ 1/4 & \text{update} \end{cases}, \quad (19)$$

and

$$q(\mathbf{z}'|k', \mathbf{z}) = \begin{cases} 1/\Delta z & \text{birth} \\ 1/(k-1) & \text{death} \\ \frac{1}{k-1} \times \frac{1}{\sqrt{2\pi}\Sigma_z} \exp\left[-\frac{(z'-z)^2}{2\Sigma_z^2}\right] & \text{move} \\ 1 & \text{update} \end{cases}, \quad (20)$$

and

$$q(\boldsymbol{\sigma}'|k', \boldsymbol{\sigma}) = \begin{cases} \frac{1}{2} \times \frac{1}{\sqrt{2\pi}\Sigma_\sigma} \exp\left[-\frac{(\sigma'-\sigma)^2}{2\Sigma_\sigma^2}\right] & \text{birth} \\ 1/2 & \text{death} \\ 1 & \text{move} \\ \frac{1}{k} \times \frac{1}{\sqrt{2\pi}\Sigma_\sigma} \exp\left[-\frac{(\sigma'-\sigma)^2}{2\Sigma_\sigma^2}\right] & \text{update} \end{cases}, \quad (21)$$

where Σ_z and Σ_σ are the standard deviations for perturbing the layer interface depths and conductivities. Because the reverse of the birth is a death, the form for $q(\mathbf{m}|\mathbf{m}')$ can be easily obtained.

2.3.3 Acceptance probabilities

Substituting eqs (12) and (18) into eq. (17), and ignoring the Jacobian $|\mathbf{J}|$, the acceptance probability $\alpha(\mathbf{m}'|\mathbf{m})$ becomes

$$\alpha(\mathbf{m}'|\mathbf{m}) = \min \left[1, \frac{p(\mathbf{d}|\mathbf{m}')}{p(\mathbf{d}|\mathbf{m})} \frac{p(k')p(\mathbf{z}'|k')p(\sigma'|k')}{p(k)p(\mathbf{z}|k)p(\sigma|k)} \frac{q(k|k')q(\mathbf{z}|k, \mathbf{z}')q(\sigma|k, \sigma')}{q(k'|k)q(\mathbf{z}'|k', \mathbf{z})q(\sigma'|k', \sigma)} \right]. \quad (22)$$

Using eqs (13) and (14) and eqs (19)–(21), we obtain the acceptance probabilities for the birth perturbation:

$$\alpha(\mathbf{m}'|\mathbf{m}) = \min \left\{ 1, \frac{p(\mathbf{d}|\mathbf{m}')}{p(\mathbf{d}|\mathbf{m})} \frac{p(\sigma'|k')}{p(\sigma|k)} \sqrt{2\pi \Sigma_\sigma} \exp \left[\frac{(\sigma' - \sigma)^2}{2\Sigma_\sigma^2} \right] \right\}, \quad (23)$$

for the death perturbation:

$$\alpha(\mathbf{m}'|\mathbf{m}) = \min \left\{ 1, \frac{p(\mathbf{d}|\mathbf{m}')}{p(\mathbf{d}|\mathbf{m})} \frac{p(\sigma'|k')}{p(\sigma|k)} \frac{1}{\sqrt{2\pi \Sigma_\sigma}} \exp \left[-\frac{(\sigma - \sigma')^2}{2\Sigma_\sigma^2} \right] \right\}, \quad (24)$$

and for the move and update perturbations:

$$\alpha(\mathbf{m}'|\mathbf{m}) = \min \left\{ 1, \frac{p(\mathbf{d}|\mathbf{m}')}{p(\mathbf{d}|\mathbf{m})} \frac{p(\sigma'|k')}{p(\sigma|k)} \right\}, \quad (25)$$

where $\frac{p(\mathbf{d}|\mathbf{m}')}{p(\mathbf{d}|\mathbf{m})}$ can be computed using eq. (11) by forward modelling, $\frac{p(\sigma'|k')}{p(\sigma|k)}$ is computed using eq. (15) for the uniform prior and (16) for the smooth prior.

2.3.4 Parallel implementation

We have implemented the above trans-dimensional Bayesian inversion algorithm into a standalone C++ code. To accelerate the computations, we have parallelized the code using MPI. The code can simultaneously run a large number of Markov chains with different initial models. To adequately sample the model space, each Markov chain will iterate hundreds of thousands of times. To ensure that stationary sampling in high-probability regions has been reached, the initial section of the Markov chain is discarded as the burn-in period. The models after the burn-in period will be output and displayed with Python.

3 SYNTHETIC DATA TESTS

The synthetic data tests aim to (1) investigate the resolutions of MT and GDS responses; (2) demonstrate how joint inversion of MT and GDS responses reduces the model uncertainty; and (3) investigate how different prior distributions of layer conductivities affect the posterior model distributions. For the following tests, the number of layers $k = [2, 30]$, layer interface depths $z = [0, 2000]$ km, and layer conductivities $\sigma = [10^{-4}, 10^2]$ S/m.

3.1 Effects of separate and joint inversions

To investigate the resolutions of MT and GDS responses and demonstrate how joint inversion reduces the model uncertainty, we first apply our trans-dimensional MCMC algorithm to a globally averaged layered conductivity model [Fig. 2(a)]. This model was derived by Kuvshinov *et al.* (2021) using satellite-detected tidal magnetic signals and magnetospheric Q -responses. From Earth's surface down to 2000-km depth, the conductivity values change by nearly four orders of magnitude. Therefore, it should be suitable for investigating the resolutions of different data. The synthetic MT apparent resistivity and phase with a total of 20 logarithmically spaced periods from 1 to 7200 s, ionospheric (hereafter referred to as Sq) G2L TFs with six periods of $24/p$ ($p = 1, 2, \dots, 6$) h, and satellite magnetospheric (hereafter referred to as Dst) Q_1 -response with 20 logarithmically spaced periods from 2 to 100 d were generated by adding 3 per cent Gaussian noise to the model responses [Figs 2(b)–(d)].

The synthetic MT and GDS responses were inverted separately and jointly using the trans-dimensional MCMC algorithm. The smooth prior (16) with prior covariance being 0.5 was adopted. We ran six Markov chains with different initial models simultaneously on a PC with one Intel Core i7-10750H CPU (six cores) and 16 GB RAM. The number of MCMC iterations was set to 1 million for each chain. The MCMC run time for the MT-only, Sq-only, Dst-only and joint inversions are only about 17, 8, 18 and 53 s, respectively.

To determine the length of the burn-in period and check the convergence of the inversion, we illustrate in Fig. 3(a) the convergence curves of the root mean square (RMS) misfit as a function of the number of samples. The histograms of RMS data misfit for all accepted models are shown in Fig. 3(b). First, we observe that the initial RMS values for all chains are different. This observation demonstrates that all chains are initialized with different states, which helps escape the local minima. Secondly, all chains converge rapidly within several thousand iterations, and the RMS data misfit does not change appreciably after 10 000 iterations. Thirdly, the RMS misfit values for the separate and joint inversions are around 1.0, and the models fit the observed data within uncertainties (Fig. 2). These observations indicate the convergence of the Markov chains and we set the burn-in period to 10 000. After the burn-in period, every 100th model is saved to reduce the storage requirements and the correlation of accepted models.

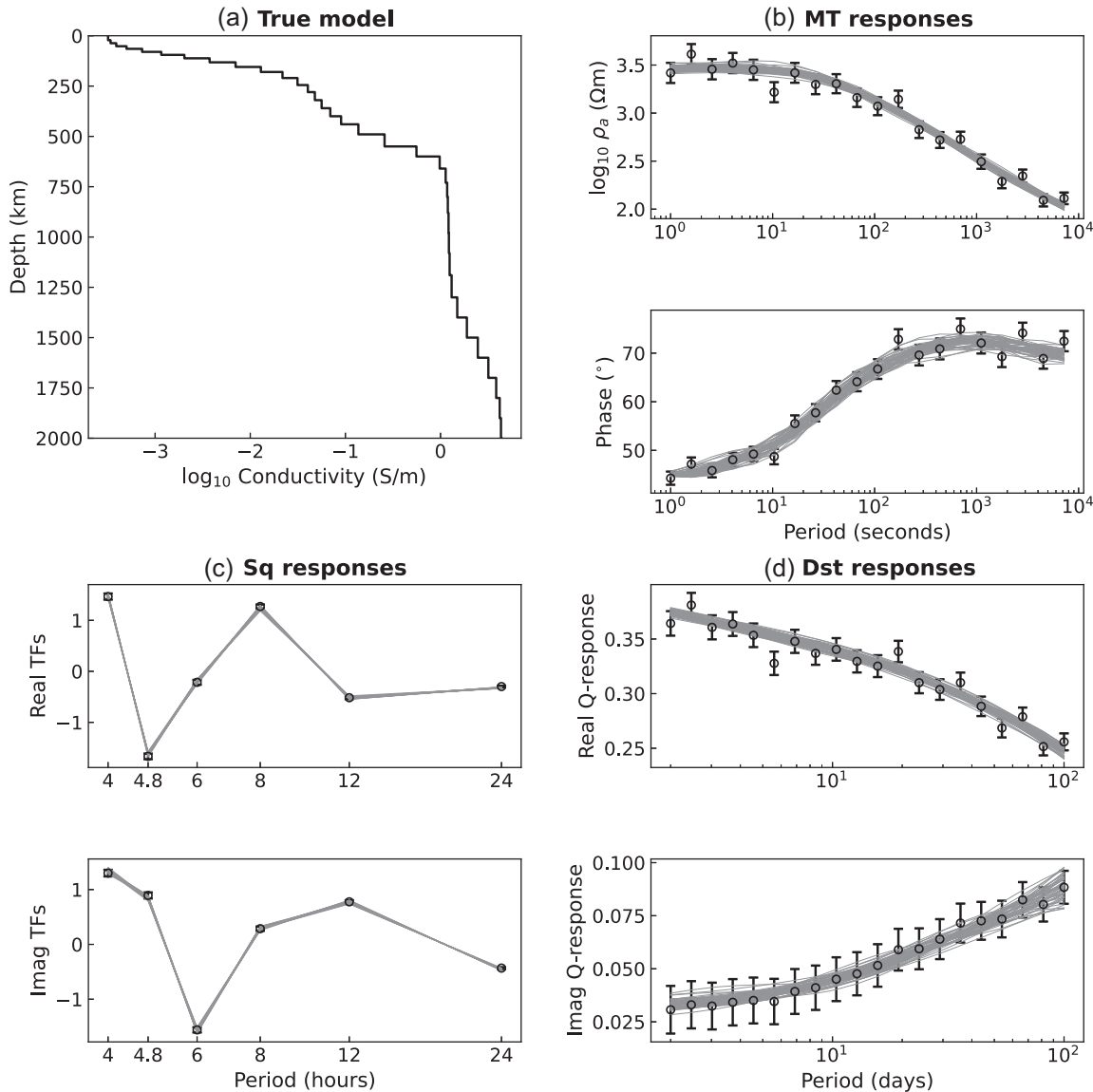


Figure 2. (a) Illustration of the layered Earth conductivity model derived by Kuvshinov *et al.* (2021) and the corresponding synthetic (b) MT apparent resistivity and phase, (c) Sq G2L TFs, and (d) satellite Dst Q -response. The error bars denote the data uncertainties. The grey lines denote the predicted model responses for 50 randomly selected conductivity models of the joint posterior model distribution [Fig. 4(d)].

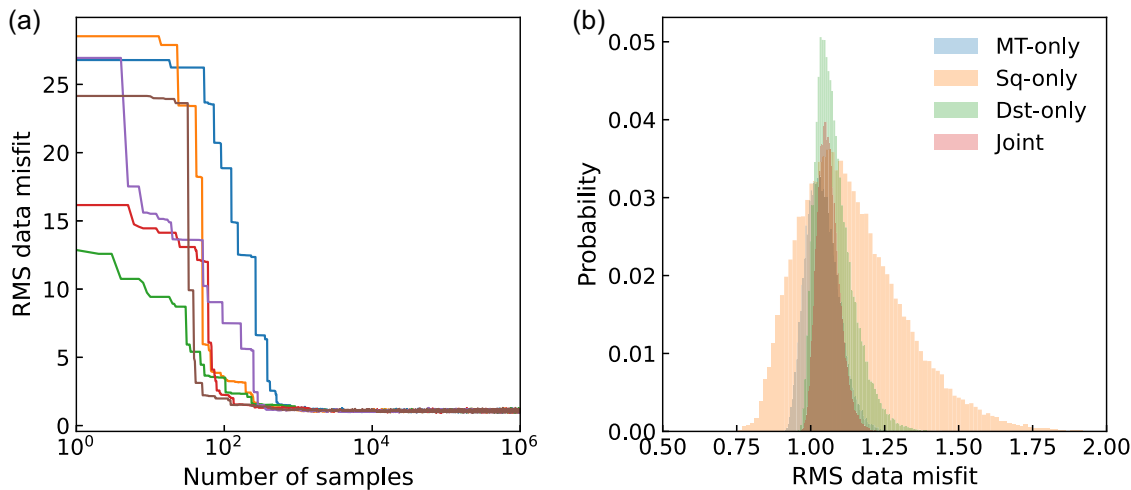


Figure 3. (a) Convergence curves of the RMS data misfit of six chains for the joint inversion and (b) the histograms of RMS data misfit for the accepted models.

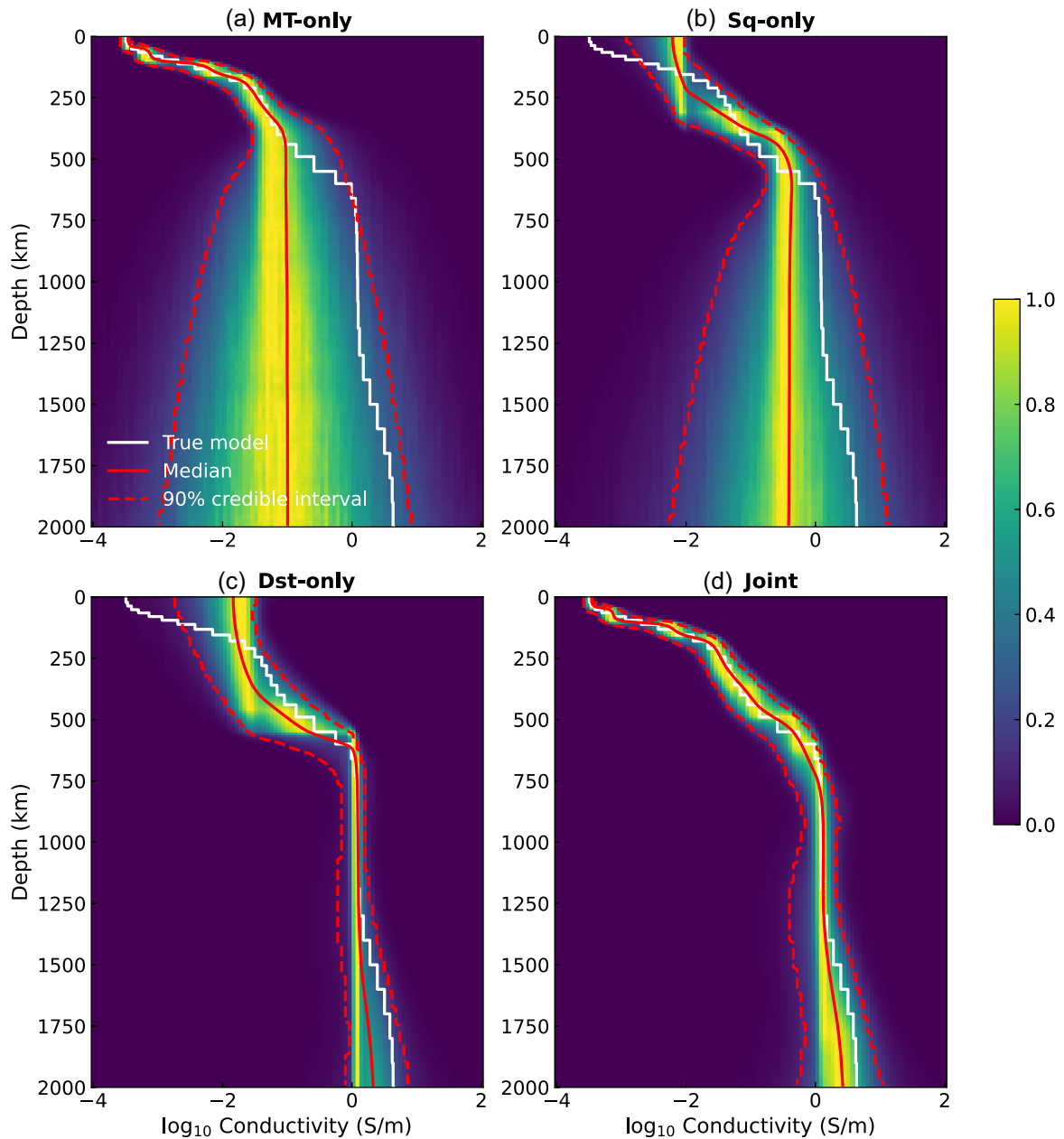


Figure 4. Posterior probability distributions of layer conductivities for the (a) MT-only, (b) Sq-only, (c) Dst-only and (d) joint inversions. The warmer and cooler colours indicate higher and lower probabilities, respectively. The white line denotes the true model and the red solid line indicates the posterior median model. The left and right red dash lines indicate the 5th and 95th percentiles at the corresponding depth, which corresponds to the 90 per cent credible interval.

Fig. 4 summarizes the posterior probability distributions of layer conductivities for the MT-only, Sq-only, Dst-only and joint inversions. Above 400-km depths, the MT responses constrain the true conductivity structures with a narrow 90 per cent credible interval, the preferred posterior median model is in good agreement with the true model, suggesting that the upper mantle conductivity structures are well constrained by the MT-only inversion. Below the upper mantle, the conductivity structures are poorly constrained with a broad credible interval. We note that for field data applications, if long-period electric potential data can be measured accurately, such as by the submarine cable (Lizarralde *et al.* 1995; Utada *et al.* 2003; Shimizu *et al.* 2010) or telephone lines (Egbert *et al.* 1992; Ichiki *et al.* 2001), longer period MT responses can be estimated, allowing us to probe the transition zone and middle mantle. The ionospheric Sq data constrains the true conductivity structures reasonably well at depths between 100 and 600 km. The magnetospheric Dst responses can constrain the true conductivity structures from the mantle transition zone down to the lower mantle. However, all separate inversions fall to recover the true conductivity structures at all depths. Compared to the separate inversion, joint inversion has successfully recovered the true conductivity model with a narrower credible interval [Fig. 4(d)], indicating an enhanced resolution and decreased uncertainty.

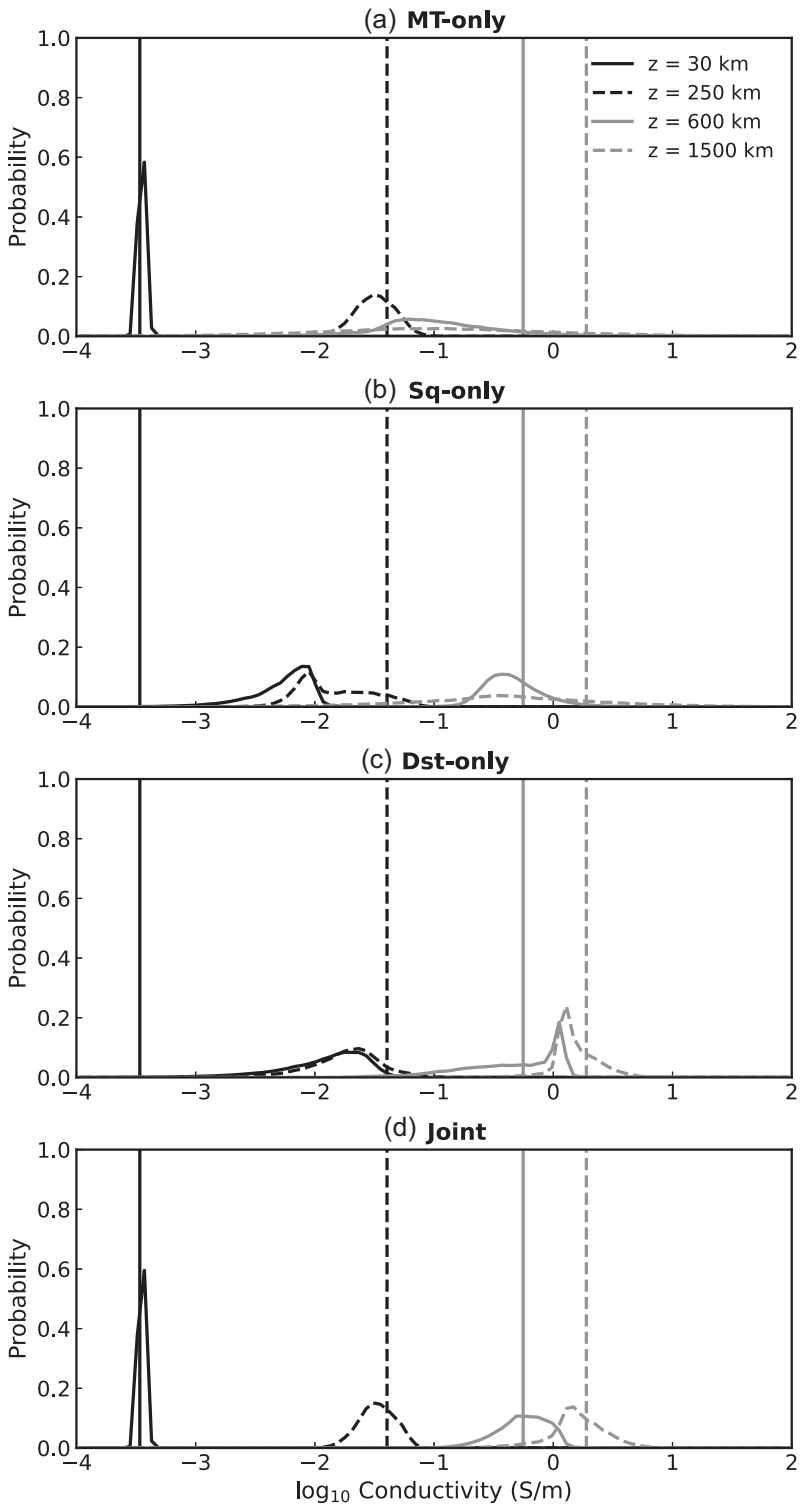


Figure 5. Posterior probabilities of conductivity at different depths for the (a) MT-only, (b) Sq-only, (c) Dst-only and (d) joint inversions. The true conductivity values at the corresponding depths are denoted by vertical lines.

To see more details of data resolutions and model uncertainties, we show in Fig. 5 the posterior probability of conductivity at four different depths: 30, 250, 600 and 1500 km. For the MT responses, a distinct probability peak near the true value is observed at 30 km, indicating a good resolution and small uncertainty. At 250 km, the probability peak becomes broader. At 600- and 1500-km depths, no distinct peaks are observed. These results suggest a loss of resolution with depths, which is due to the diffusion nature of long-period EM fields. Compared to the MT responses, the ionospheric Sq and magnetospheric Dst responses show relatively poorer resolutions. Joint inversion shows distinct probability peaks near the true conductivity values, indicating significantly improved resolution.

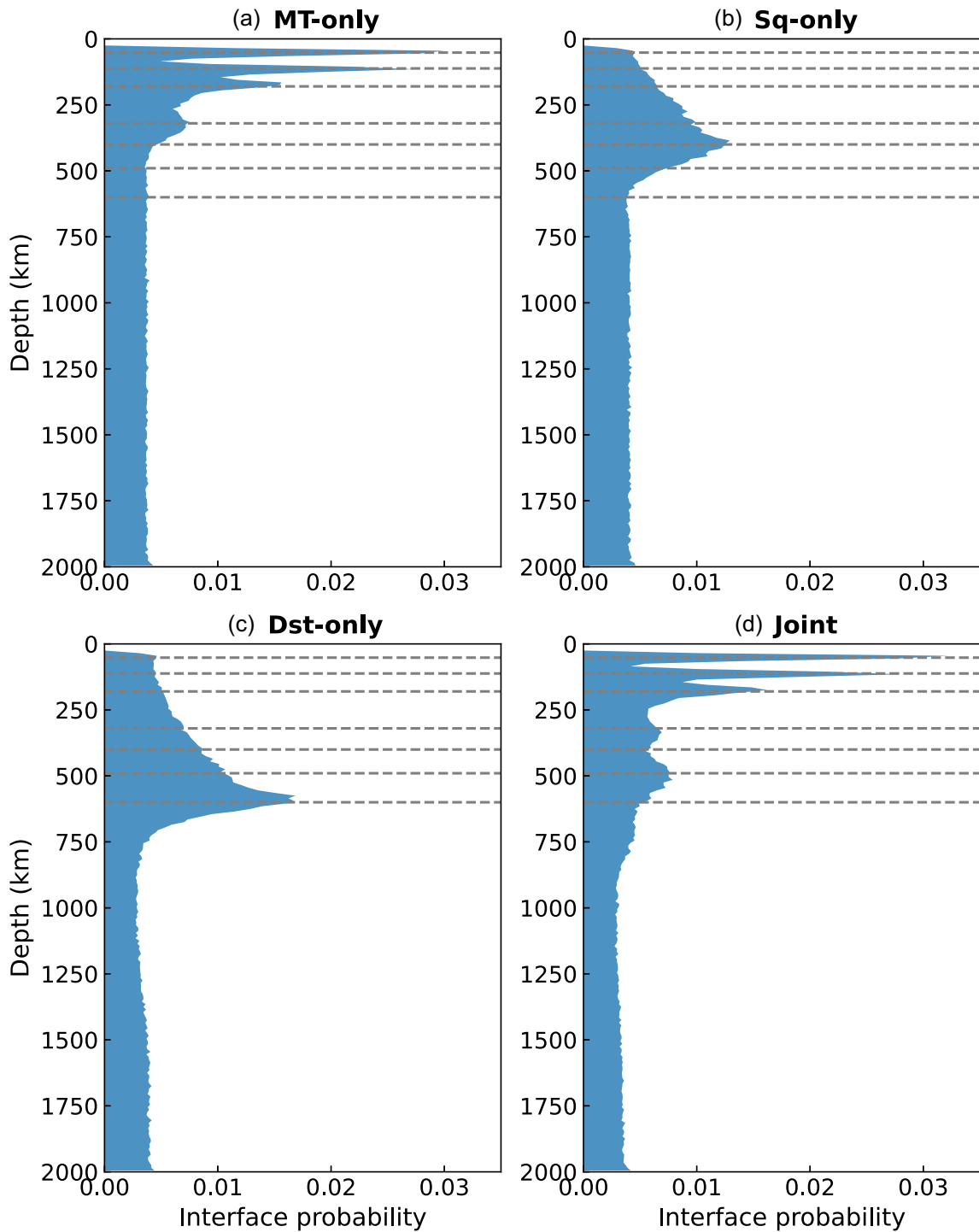


Figure 6. Interface depth probabilities for the (a) MT-only, (b) Sq-only, (c) Dst-only and (d) joint inversions. The grey dash lines denote the preset interface depths (52, 112, 180, 320, 400, 490 and 600 km) of the synthetic model.

Fig. 6 shows the probability of layer interface depths with several preset interface depths (52, 112, 180, 320, 400, 490, 600 km) are denoted in grey dash lines. For both separate and joint inversions, distinct interface peaks are observed. These peaks suggest the depths of layer interfaces and the corresponding conductivity jumps at these interfaces. The shallow interfaces have higher probabilities and the deep interfaces have lower and nearly uniform probabilities, indicating again the loss of resolution. The MT data only resolves the shallow interfaces while the GDS data only resolves the deep interfaces. Compared to the separate inversion, the joint inversion recovers most of the preset layer interfaces. The number of layer interfaces determined by the trans-dimensional MCMC algorithm is considerably less than that of the true model. This is related to two reasons: first, the true conductivity model shows smooth conductivity changes; due to the diffusion

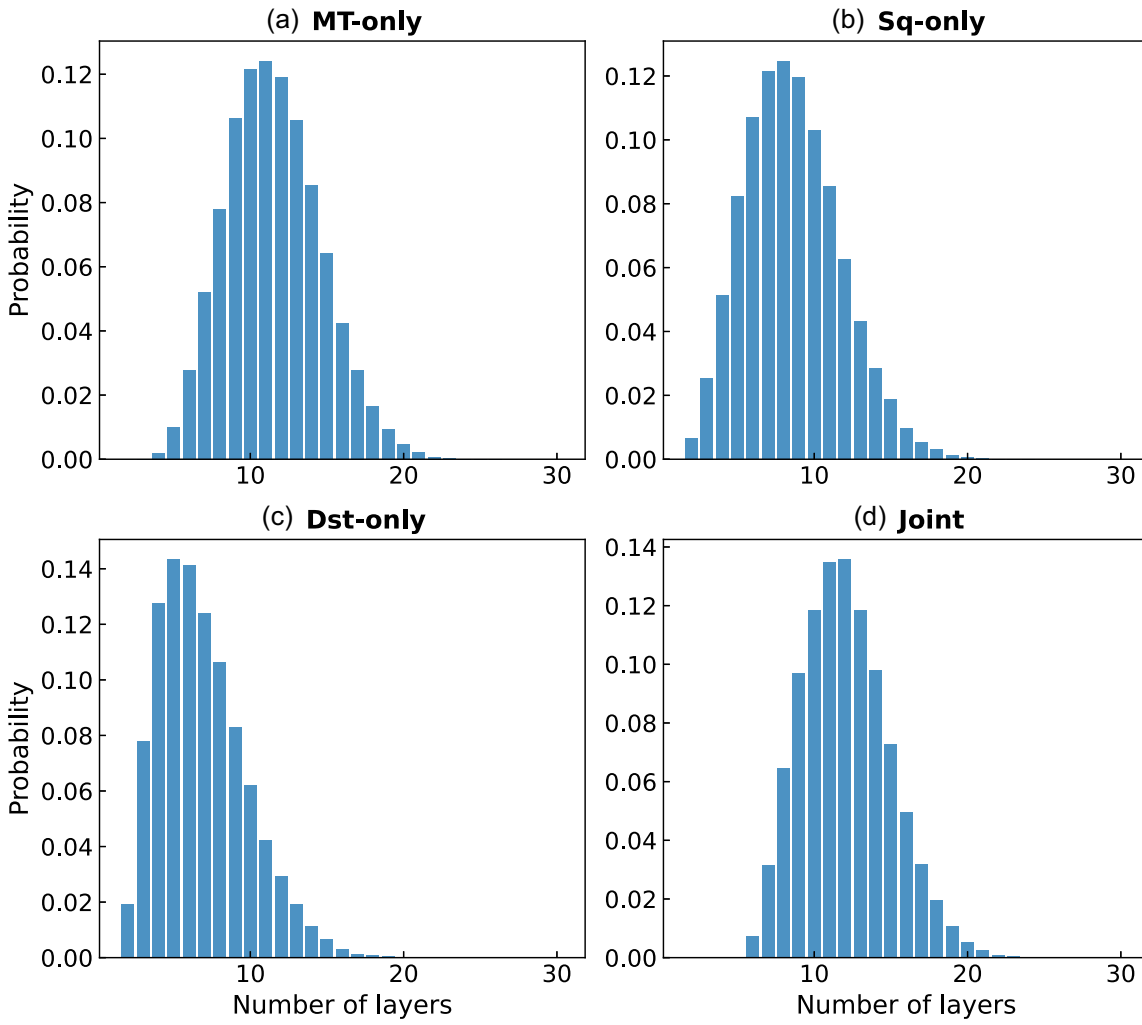


Figure 7. Histograms of the number of layers for the (a) MT-only, (b) Sq-only, (c) Dst-only and (d) joint inversions.

nature of EM fields, thin layers can not be distinguished by the MT and GDS responses. Secondly, the trans-dimensional MCMC algorithm only generates structures that are needed by the data through self-parametrizing the model parameters. We will discuss this issue later for a blocky model with sharp conductivity changes.

A further discussion is on the parsimony criterion of the trans-dimensional MCMC algorithm. Fig. 7 shows the histograms of the number of layers. Compared to the MT responses, models with fewer layers are preferred for the GDS Sq and Dst responses. One possible explanation is that, when the period increases, the wavelength becomes larger, resulting in the loss of resolution. From surface to 2000 km, the true model is parametrized with 37 layers. The most probable number of layers for the MT-only, Sq-only, Dst-only and joint inversions are 11, 8, 5 and 12, respectively, which are much less than the true number of layers. This result demonstrates the parsimony criterion of the trans-dimensional MCMC algorithm (Malinverno 2002), that is, the models with fewer layers have much higher probabilities to be accepted.

The above tests demonstrate that the joint inversion can combine complementary information provided by the MT and ionospheric and magnetospheric GDS responses. To obtain reliable crustal and mantle conductivity structures, joint inversion of MT and GDS responses is necessary.

3.2 Effects of different prior distributions of layer conductivities

To investigate how different prior distributions of layer conductivities affect the posterior model distributions, we consider two different conductivity models. The first model and synthetic data set are taken from the above tests; this model is denoted as the 'smooth model'. The second model has sharp conductivity changes; this model is denoted as the 'blocky model' [Fig. 8(a)]. The synthetic MT and GDS responses for the blocky model were generated by adding 3 per cent Gaussian noise to the model responses for the same periods as the above tests [Figs 8(b)–(d)].

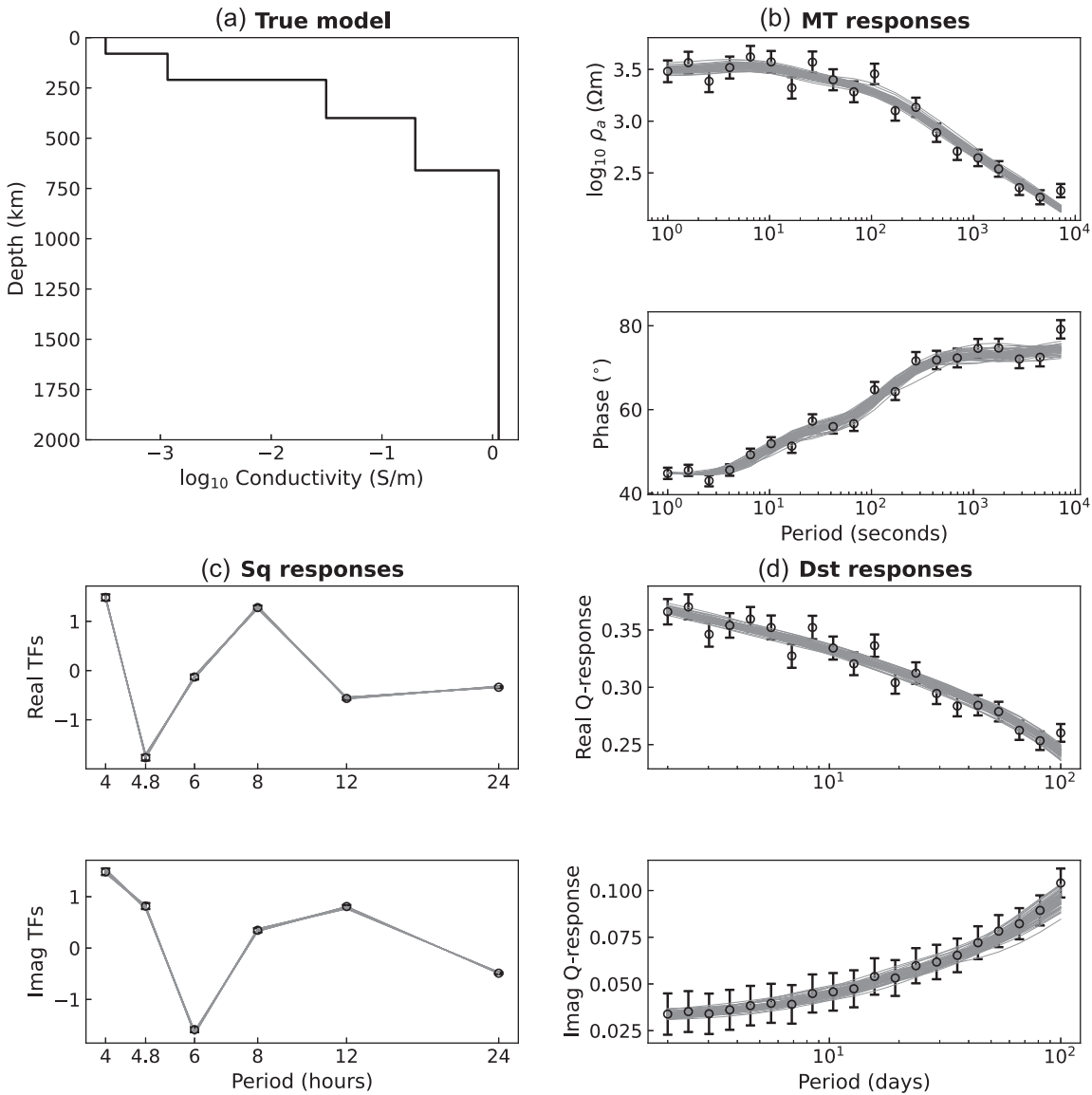


Figure 8. Similar to Fig. 2, but for the blocky model with sharp conductivity changes.

We inverted the synthetic MT and GDS responses jointly for the following three cases. (1) *uniform prior*: the uniform prior distribution (15) was used; (2) *smooth prior 1.0*: the smooth prior distribution (16) with prior covariance being 1.0 was used; (3) *smooth prior 0.5*: the smooth prior distribution (16) with prior covariance being 0.5 was used.

A total of six Markov chains were run simultaneously. Fig. 9(a) shows the convergence of the RMS misfit as a function of the number of samples. Fig. 9(b) shows the corresponding histograms of RMS data misfit. For both the smooth and blocky models, the RMS misfit values for all chains decrease rapidly, and the final RMS values for the three priors are around 1.0, suggesting the convergence of the chains is reached. The burn-in period is set to 10 000.

Fig. 10 shows the posterior conductivity distributions for the smooth and blocky models. Despite the noise in the synthetic data, the true model is bounded by the 90 per cent credible interval for all priors. The posterior median model is in good agreement with the true model. The uniform prior only gives the minimum and maximum allowable conductivities. Therefore, when the data lack resolution, the corresponding model uncertainties are large and the models are poorly constrained [Figs 10(a) and (d)]. The uniform prior also generates conductivity models with unrealistic oscillations since the prior information of layer conductivities gives little information. By using the smooth prior, which constrains the smoothness of layer conductivities between adjacent layers, these oscillations are efficiently suppressed. Smaller prior covariance generates smoother inverse models and smaller uncertainties, reflecting the reduced model space due to smooth constraints.

Fig. 11 illustrates the posterior probability of conductivity at different depths. For the smooth model, when using the uniform prior and the smooth prior 1.0, two probability peaks are observed at 600-km depth, indicating that the true conductivity value is poorly constrained.

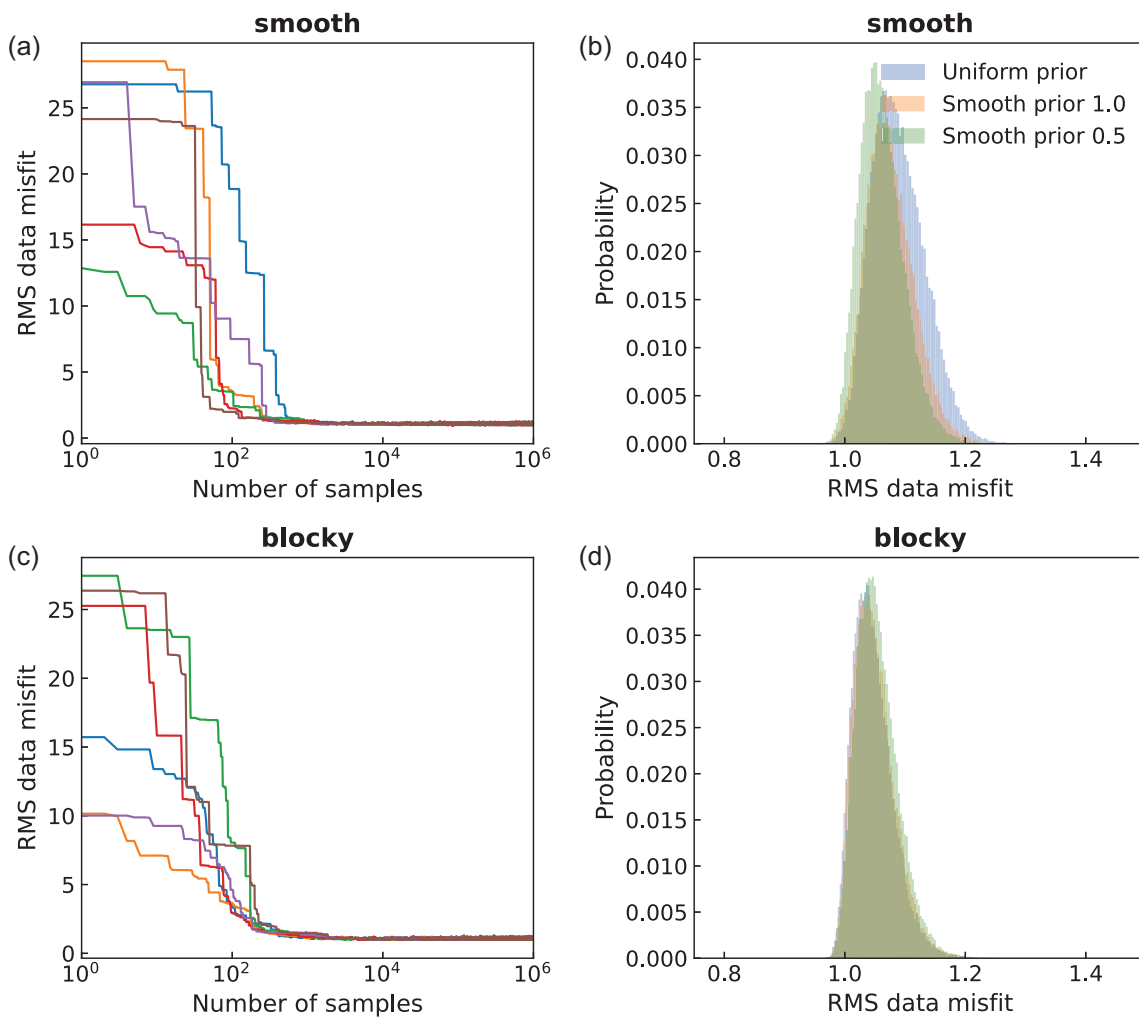


Figure 9. Convergence curves of the RMS data misfit of six chains for the smooth prior 0.5 (left) and the histograms of RMS data misfit for the accepted models (right). Panels (a) and (b) denote the results for the smooth model, and panels (c) and (d) denote the results for the blocky model.

After applying the smooth prior with prior covariance being 0.5, one distinct peak centred at the true conductivity value is obtained. For the blocky model, the true conductivity values are recovered almost equally well for the three priors.

Fig. 12 shows the probability of layer interface depths. For both the smooth and blocky models, although the interface probability values are different for the three priors, distinct interface probability peaks are still observed at the preset interface depths. Notably, no constraints on the interface depths during inversion and the conductivity jumps are resolved automatically by the trans-dimensional MCMC algorithm, indicating the advantage of the trans-dimensional Bayesian inversion in detecting conductivity discontinuities in the Earth's interior. This observation also implies that using different priors will not affect the trans-dimensional MCMC algorithm's ability to automatically determine the interface depths for both smooth and blocky models.

Consequently, we choose the smooth prior as our preferred approach since it can generate geologically meaningful models while allowing for conductivity jumps.

4 APPLICATION TO FIELD DATA AT TUCSON OBSERVATORY

4.1 Data processing

Tucson geomagnetic observatory is located in southwestern North America. For the MT responses at Tucson observatory, we use the very long period apparent resistivity and phase from 0.19 to 5 d [Fig. 13(a)], which were derived by Egbert *et al.* (1992) from a scalar impedance using 11 yr of electric potential data together with the geomagnetic data recorded by the Tucson observatory. For the estimation of the scalar MT impedance, we refer to Egbert *et al.* (1992).

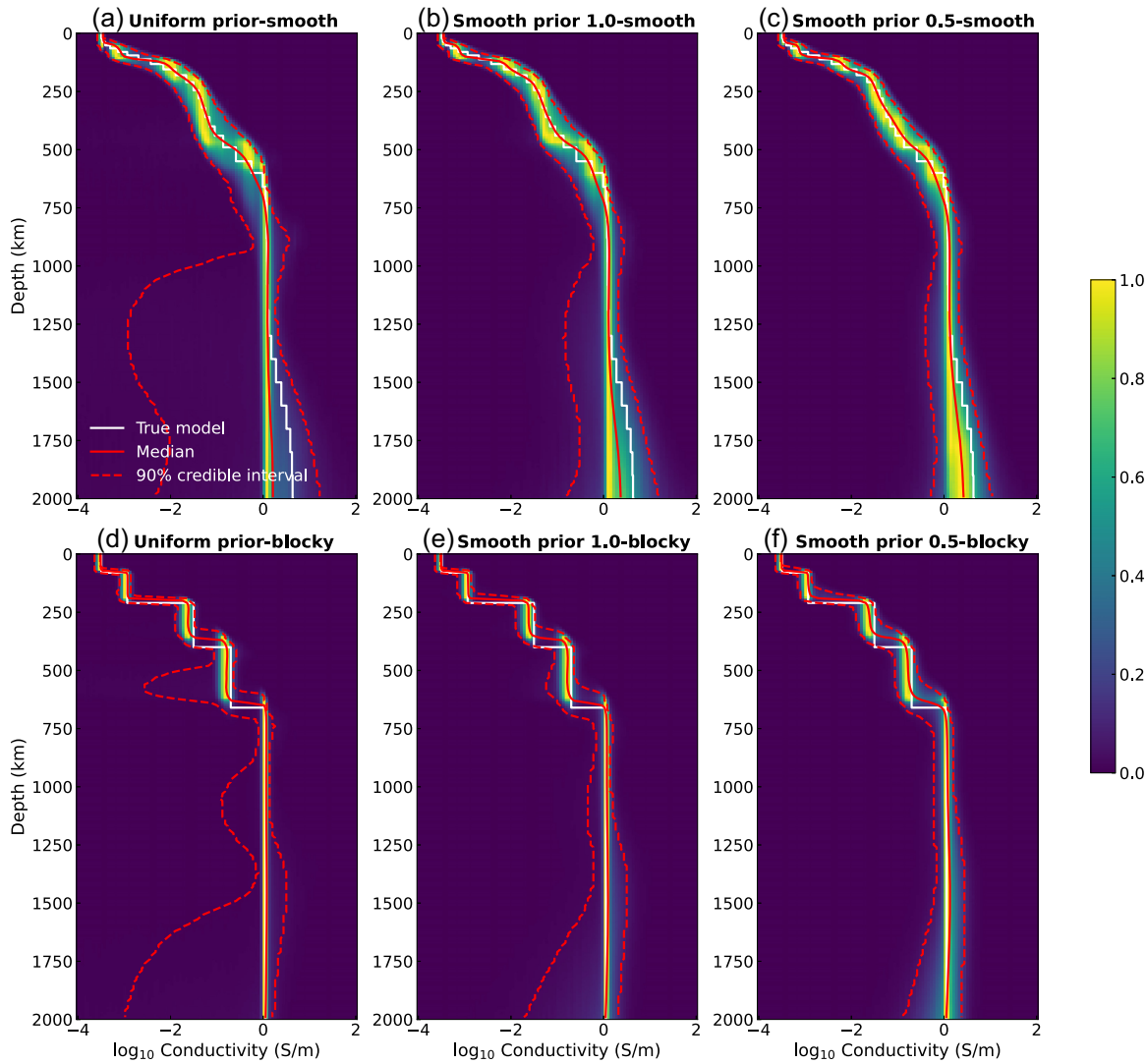


Figure 10. Posterior probability distributions of layer conductivities for inversions with (a) and (d) uniform prior, (b) and (e) smooth prior with prior covariance being 1.0 and (c) and (f) smooth prior with prior covariance being 0.5. Panels (a)–(c) denote the results for the smooth model, and panels (d)–(f) denote the results for the blocky model.

For the GDS responses at Tucson observatory (>5 d), which are dominated by the magnetospheric ring current, we employ the C -response functions. Instead of using the GDS responses of Egbert *et al.* (1992) estimated from 46 yr of geomagnetic data, we re-estimate the GDS C -responses using more than 100 yr (1919–2020) of Tucson geomagnetic observatory data. Using more data allows us to obtain more reliable long-period GDS responses. The new GDS C -responses were estimated by the following procedures:

- (1) We collected the hourly mean value of three geomagnetic field components for Tucson observatory (1919–2020) from the quality-controlled British Geological Survey data base (Macmillan & Olsen 2013).
- (2) We removed main field and secular variations from raw time times using the IGRF-13 geomagnetic field model (Alken *et al.* 2021).
- (3) We rotated the horizontal field components from geographic to geomagnetic coordinate systems using the geomagnetic north pole of IGRF 2015. Note that the choice of different geomagnetic north poles has only negligible effects on the final results (Semenov & Kuvshinov 2012).
- (4) We estimated C -responses in the period range 6–100 d according to eq. (6) using the section-averaging approach (Semenov & Kuvshinov 2012) and iteratively reweighted least squares method (Aster *et al.* 2018). Data uncertainty is estimated by the jackknife approach (Chave & Thomson 1989).

New C -responses are shown in Fig. 13(b). As is seen, responses are smooth over the entire period, and the data uncertainties are relatively small. The real part is positive and shows an increase with increasing periods, and the imaginary part is negative and shows a decrease with increasing periods, which is the typical behaviour of C -responses for 1D conductivity structures. These results indicate that the data quality is good and an assumption on 1D conductivity beneath Tucson geomagnetic observatory is reasonable (Semenov & Kuvshinov 2012).

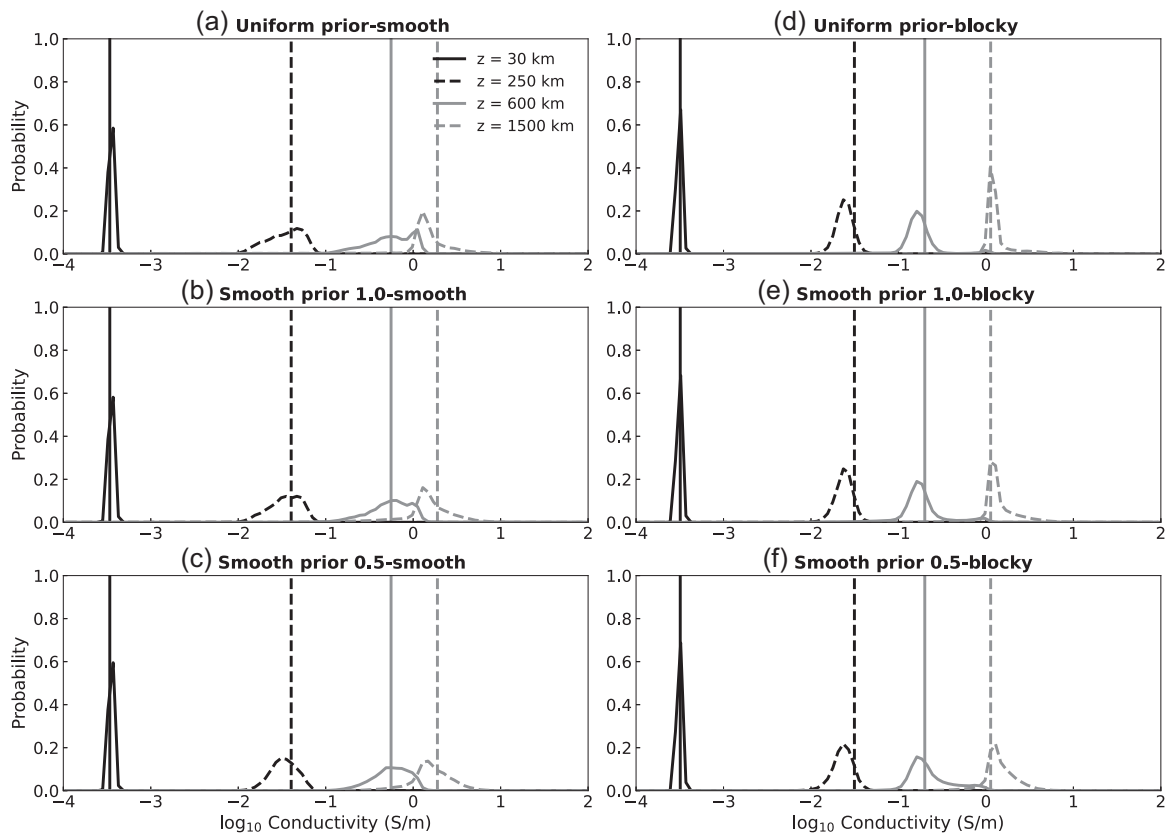


Figure 11. Similar to Fig. 10, but for the posterior probabilities of conductivity at different depths.

4.2 Effects of MT data errors on the posterior model distributions

As discussed in Egbert *et al.* (1992), the MT apparent resistivity and phase are individually but not mutually consistent with 1D conductivity distributions. Therefore, an appropriate assumption of data errors is critical for obtaining reliable 1D conductivity structures. Before jointly inverting the MT and GDS responses for the final conductivity models, we first investigate the effects of the assumption of MT data errors on the posterior model distributions.

Six MT data sets are considered. Data set 1 contains all periods of data (0.19–5 d) with default errors of Egbert *et al.* (1992). Data set 2 only contains the data at periods less than 1 d with default errors. Data set 3 only contains the data at periods of 1–5 d with default errors. Data set 4 contains all periods of data with an error floor of 3.5 per cent for the apparent resistivity and 1° for the phase. Data set 5 contains all periods of data with an error floor of 5 per cent for the apparent resistivity and 1.5° for the phase. Data set 6 contains all periods of data with an error floor of 10 per cent for the apparent resistivity and 2° for the phase.

These data sets were inverted with six chains simultaneously. The number of MCMC iterations was two millions for each chain. Fig. 14(a) illustrates the convergence curves of the RMS data misfit for the above six data sets as a function of the number of samples. For all data sets, all chains converge rapidly. The burn-in period is set to a relatively large value of 200 000. The corresponding histograms of RMS data misfit for the final accepted models are shown in Fig. 14(b). For the inversion using all periods of data with default errors (data set 1), although the RMS misfits have decreased significantly for all chains, the final RMS misfits are relatively large. The most probable RMS misfit is about 3.6. Using subsets of data (data sets 2–3) results in smaller RMS misfits. The most probable RMS misfits for data sets 2 and 3 are around 1.9 and 1.7, respectively. By assigning a gradually increased error floor for the apparent resistivity and phase (data sets 4–6), the resulting RMS misfit decreases gradually. The RMS misfit for data set 6 is around 1.14, which is close to 1.0.

Fig. 15 summarizes the corresponding posterior model distributions. We find that very large conductivity values of several tens of S/m at depths 700–2000 km are observed for data sets 1 and 2, which is inconsistent with previous global conductivity studies (Kelbert *et al.* 2009; Semenov & Kuvshinov 2012). This result may be caused by the poor data fit for data set 1 and the lack of resolution for data set 2. Inverting only the data at periods of 1–5 d (data set 3) generates more realistic lower mantle conductivity structures, but results in poor resolution in the upper mantle. These results indicate two points. First, inverting all periods of data is crucial for improving the resolution of conductivity models. Secondly, the default data errors may be inappropriate for the inversion of 1D conductivity structures. Figs 15(d) and (e) present the inversion results of assigning different error floors for the apparent resistivity and phase. We find that compared to data sets 1–5, data set 6 gives more realistic conductivity structures in the lower mantle (on the order of several S/m) without loss of resolution in the upper mantle.

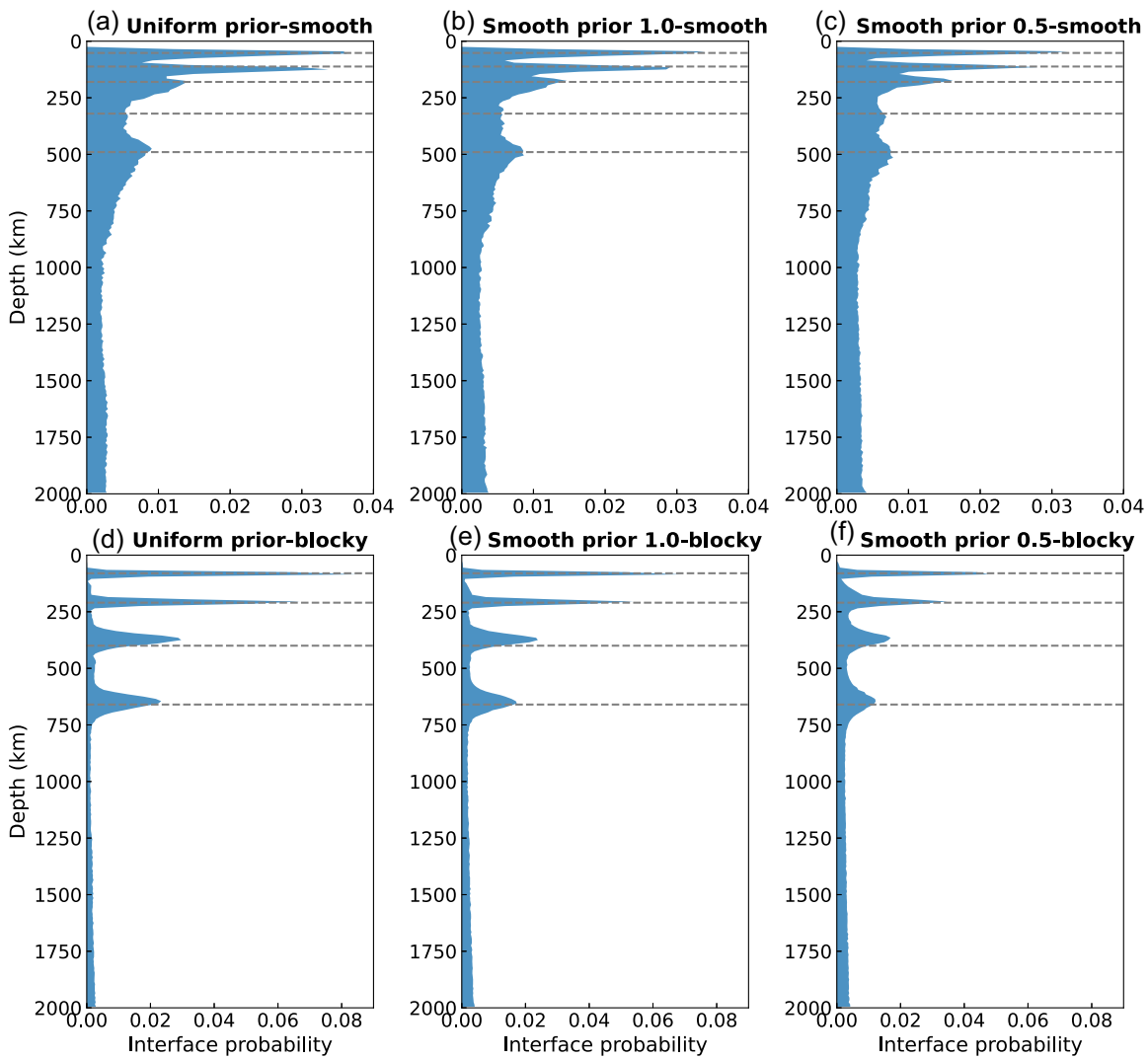


Figure 12. Similar to Fig. 10, but for the interface depth probabilities. The preset layer interface depths are denoted by grey dash lines.

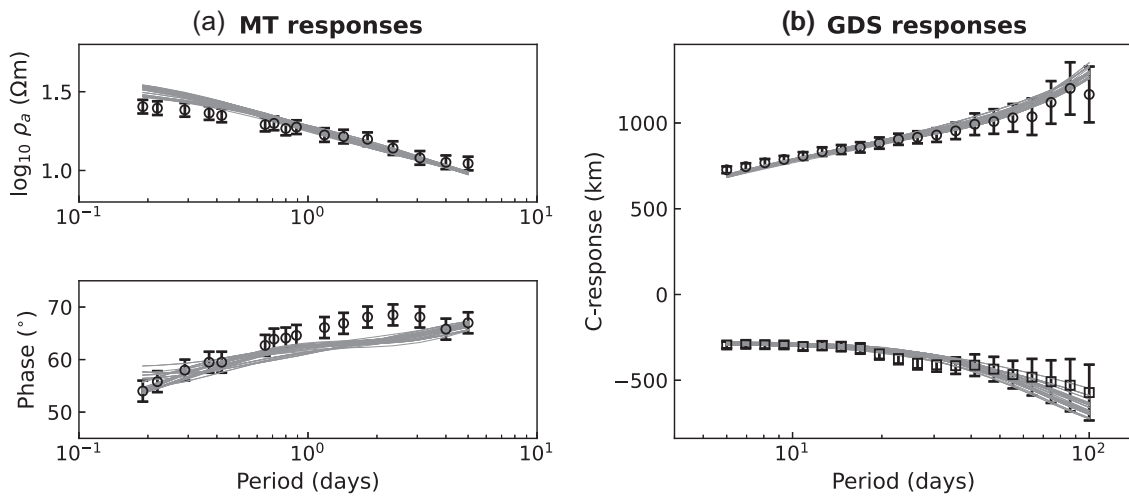


Figure 13. Field data at Tucson observatory. (a) Very long-period MT apparent resistivity and phase at Tucson observatory estimated by Egbert *et al.* (1992). An error floor of 10 per cent is used for the apparent resistivity, while that is 2° for the phase. (b) Real (circle symbols) and imaginary (square symbols) parts of the observed GDS C-response estimated in this study with error bars denoting the data uncertainties. The grey lines denote the predicted model responses for 50 randomly selected conductivity models of the joint posterior model distribution [Fig. 17(c)].

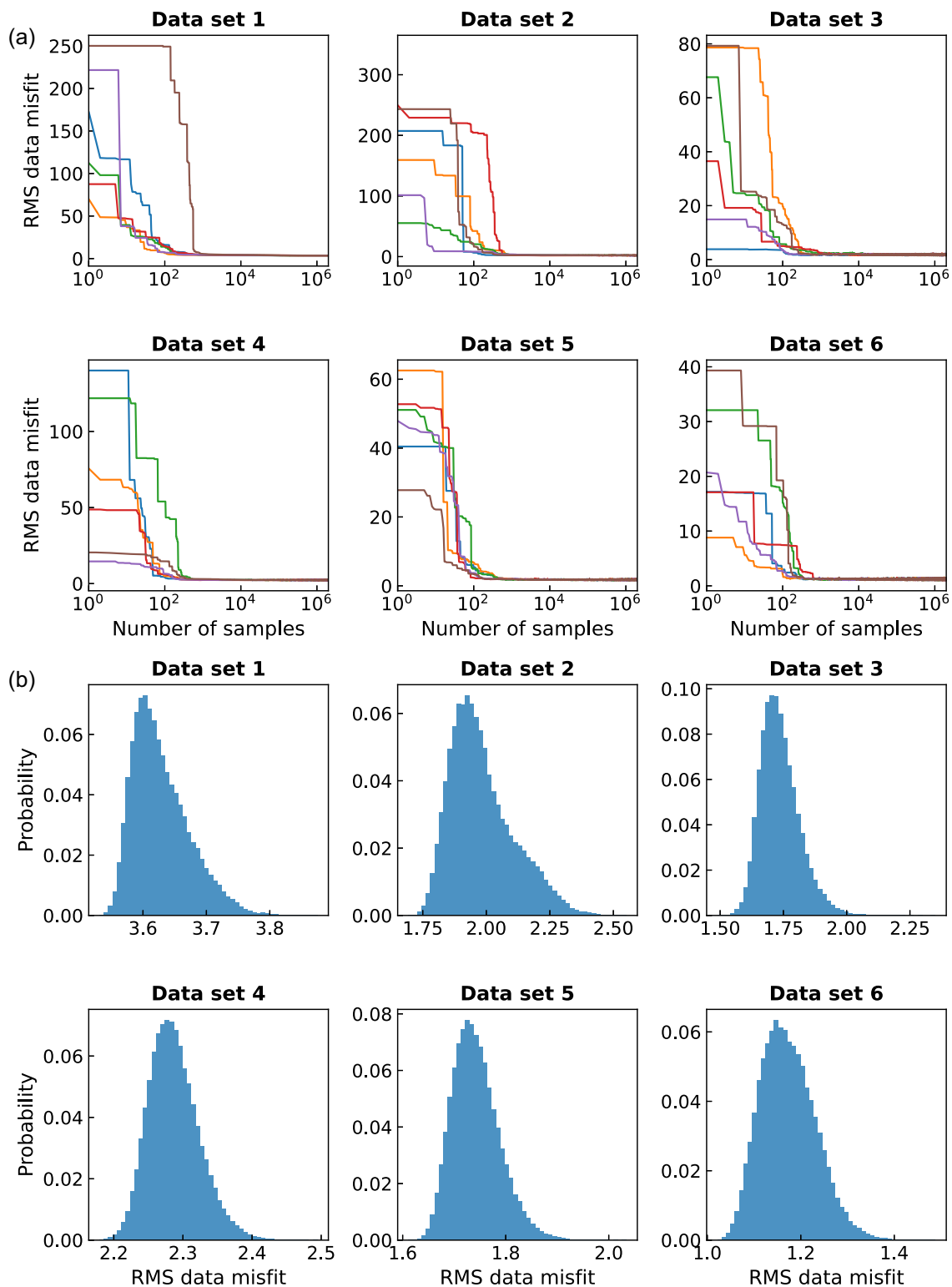


Figure 14. RMS data misfits for the investigation of the effect of MT data errors using different data sets (see main text for details). (a) Convergence curves of the RMS data misfit and (b) the histograms of RMS data misfit for the accepted models.

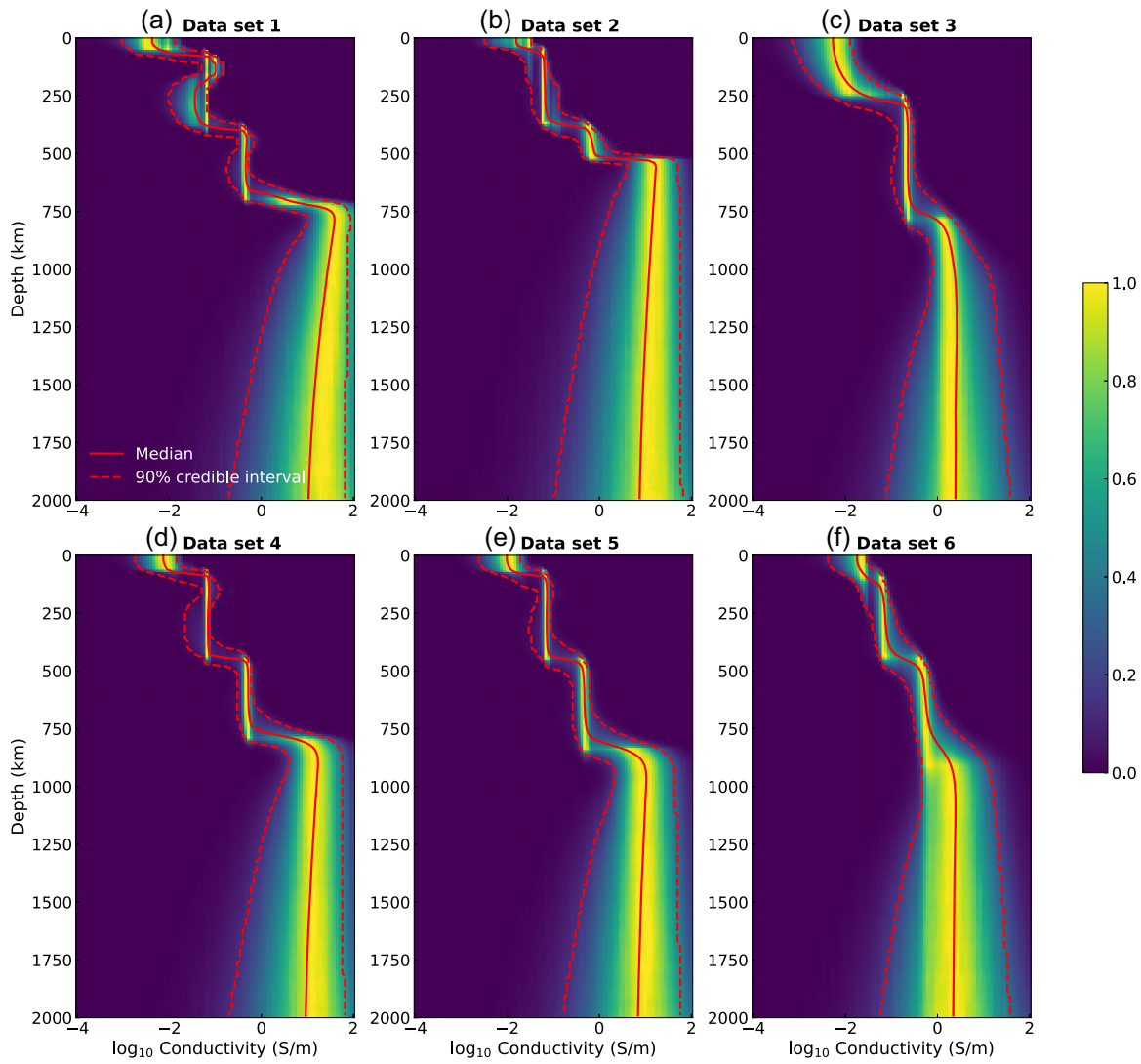


Figure 15. Posterior model distributions for the investigation of the effect of MT data errors.

The above observations suggest that assuming an error floor of 10 per cent for the apparent resistivity and 2° for the phase is appropriate. Therefore, we choose data set 6 for further discussion.

4.3 Preferred Bayesian model and its comparison with deterministic inversion

The MT and GDS responses were inverted separately and jointly using the developed trans-dimensional Bayesian code. The priors for the number of layers, interface depths and layer conductivities were $k = [2, 30]$, $z = [0, 2000]$ km and $\sigma = [10^{-4}, 10^2]$ S/m, respectively. To escape the local minima, we ran a total of 48 Markov chains simultaneously on one computing node of the High Performance Computing Center of Central South University. Each node is equipped with two Intel Xeon Gold 6248R 3.0GHz CPUs, 48 cores, and 192 GB RAM. The number of MCMC iterations was two millions for each chain. The burn-in period was set to 200–000. After the burn-in period, every 100th model was saved and assembled for the final posterior distributions. The MCMC run time for a total of 48 chains is only about 39, 66 and 125 s, demonstrating that our parallel trans-dimensional MCMC inversion algorithm can be used for efficient inversion of MT and GDS field data. For comparison, the field data were also separately and jointly inverted using the gradient-based, deterministic L-BFGS inversion code (Yao *et al.* 2022). The initial and reference models were set to 1 S/m.

Fig. 16 illustrates the histograms of RMS data misfit for the MT-only, GDS-only and joint inversions of Tucson field data. The predicted responses for 50 randomly selected inverse models estimated from Bayesian joint inversion are shown in Fig. 13. The converged RMS misfits for the Bayesian MT-only, GDS-only and joint inversions are about 1.15, 0.88 and 1.18, respectively. The corresponding RMS misfits for the deterministic L-BFGS inversion are 1.13, 1.09 and 1.15, respectively. These results suggest that both the Bayesian and L-BFGS inversion algorithms reach a reasonable data fit for the 1D inversion.

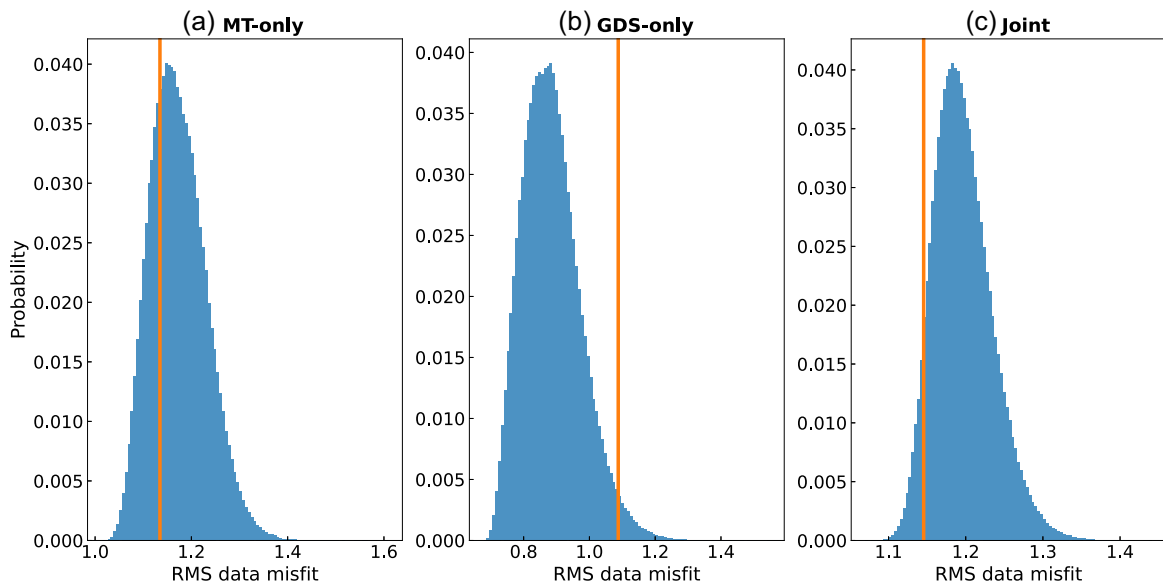


Figure 16. Histograms of RMS data misfit for the (a) MT-only, (b) GDS-only and (c) joint inversions of Tucson field data. The vertical lines indicate the corresponding RMS misfits of the deterministic L-BFGS inversion.

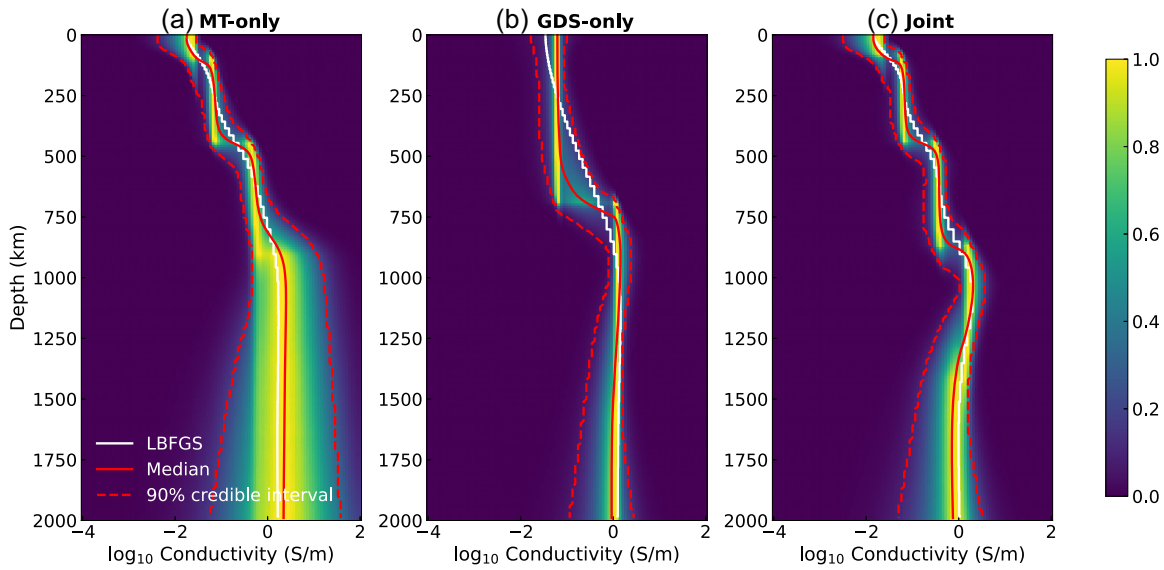


Figure 17. Posterior probability distributions of layer conductivities for the (a) MT-only, (b) GDS-only and (c) joint inversions of Tucson field data. For comparison, the corresponding L-BFGS inverse models are shown with white solid lines.

Fig. 17 shows the Bayesian posterior model distributions and the L-BFGS models. We observe that for both separate and joint inversions, the L-BFGS inverse models are well bounded by the 90 per cent credible interval and are in good agreement with the Bayesian posterior median models. The overall good agreements between the Bayesian and L-BFGS inversion results demonstrate that our trans-dimensional MCMC algorithm is well applicable to field data. We also observe that compared to the separate inversions, joint inversion of MT and GDS responses significantly improves the model resolutions and reduces the uncertainties, especially for the mantle transition zone and lower mantle.

Fig. 18 shows the interface depth probability of Bayesian inversion. The MT-only inversion generates three distinct layer interfaces, indicating a four-layered conductivity model. The GDS-only inversion generates a much simpler conductivity model, and only one distinct interface is observed. Joint inversion of MT and GDS responses generates a refined conductivity structure. Four distinct interface probability peaks are detected at around 85-, 440-, 870- and 1200-km depths [Fig. 18(c)], which is consistent with the five-layered conductivity model distribution [Fig. 17(c)].

Compared to the L-BFGS inversion and the previous deterministic joint inversion of Tucson MT and GDS responses (Egbert & Booker 1992), which only generates a preferred model, the trans-dimensional Bayesian algorithm generates both the preferred posterior median model

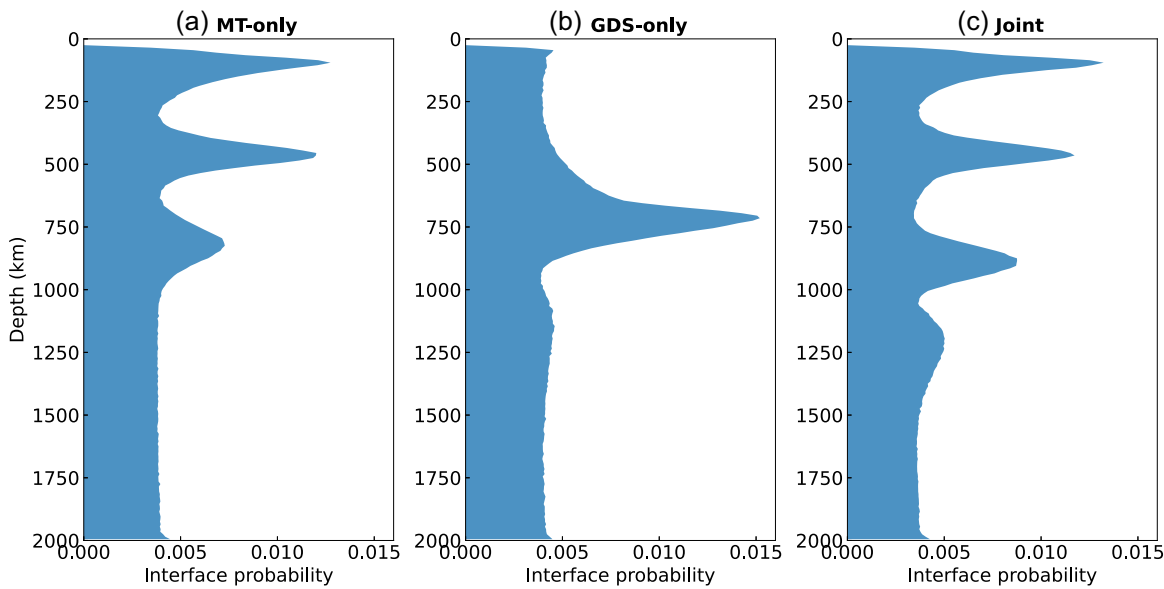


Figure 18. Interface depth probabilities for the (a) MT-only, (b) GDS-only and (c) joint inversions of Tucson field data.

as well as its uncertainty estimate. In addition, the L-BFGS models show smooth structures from the Earth's surface down to the lower mantle. Although large conductivity increases are shown, no distinct layer interfaces are observed. By automatically determining the optimal number of layers and generating a large number of models, the trans-dimensional Bayesian algorithm gives the interface depth probabilities and detects several distinct layer interfaces. Considering the detected layer interfaces, we compute the conductance (conductivity-thickness product) over 0–85, 85–440, 440–870, and 870–1200-km depth ranges for the joint posterior model distribution. The histograms of conductance are shown in Fig. 19. From the above results, we summarize the following findings concerning the crustal and mantle conductivity structures beneath Tucson: (1) Above 85 km, the conductance ranges between 50 and 2900 S with an average of ~1275 S, indicating an average conductivity of 0.015 S/m. (2) A distinct conductivity increase is observed at around 85 km. Between 85 and 440 km, the conductance ranges between 16 000 and 37 000 S with an average of ~21 300 S, indicating an average conductivity of 0.06 S/m. (3) A distinct conductivity jump is observed at around 440 km. The conductance ranges between 100 000 and 260 000 S at depths 440–870 km. The average conductance is ~167 000 S with an average conductivity of ~0.39 S/m. (4) Below 900 km, the average conductivities are of the order of 1 S/m, which is in good agreement with the previous study (Egbert & Booker 1992).

4.4 Implications of conductivity jumps

Using the trans-dimensional MCMC algorithm, a distinct interface probability peak is observed at around 85 km, which is likely related to the lithosphere-asthenosphere boundary (LAB). The narrow 90 per cent credible interval as shown in Fig. 17(c) and the high interface probability shown in Fig. 18(c) indicate that the conductivity jump at around 85 km is well constrained by the data. We further check the robustness of the conductivity jump more quantitatively by sensitivity tests. To simplify the following discussions, we adopt a simplified five-layered conductivity model (denoted as the *original model*) derived from the posterior model distribution [Fig. 17(c)]. Two modified models are considered. The model LAB1 modifies the original model by removing the conductivity jumps at 85 km. The model LAB2 reduces the conductivity jump at 85 km in half. The detailed original and modified conductivity structures are shown in Fig. 20(a) with the shade region being the 90 percent credible interval, and the forward modelling responses are shown in Figs 20(b)–(d). The corresponding RMS misfit values and the relative changes in RMS misfit for the modified models are presented in Table 2.

In Fig. 20(a), the modified models LAB1 and LAB2 are not constrained by the credible interval. Qualitatively, this observation indicates that the conductivity jump is required by the data. Although not distinct in Fig. 20(d) for the GDS responses, the MT data fit shown in Figs 20(b) and (c) illustrates that the model responses for the modified models LAB1 and LAB2 deviate from the observed data significantly. This result indicates that the upper mantle conductivity is mainly constrained by the MT data. Compared to the original model, the total RMS misfits increase by 188 per cent and 83 per cent for the modified models LAB1 and LAB2, respectively, demonstrating the high sensitivity of the data to the conductivity jump at around 85 km.

We further estimate the possible depth range of the ~85 km conductivity jump. The RMS misfits for models that vary the ~85 km conductivity jump to different depths are illustrated in Fig. 20(e). The RMS misfit is lower than that of the original model when the discontinuity depth is within 85–110 km, suggesting that the electrical LAB beneath Tucson observatory may be located in the depth range of 85–110 km. This result is in good agreement with previous seismic studies comprising Tucson region. For examples, Li *et al.* (2007) revealed an average LAB depth of ~70 km beneath the western United States using *S* receiver functions. Abt *et al.* (2010) interpreted the negative *Sp* phases at

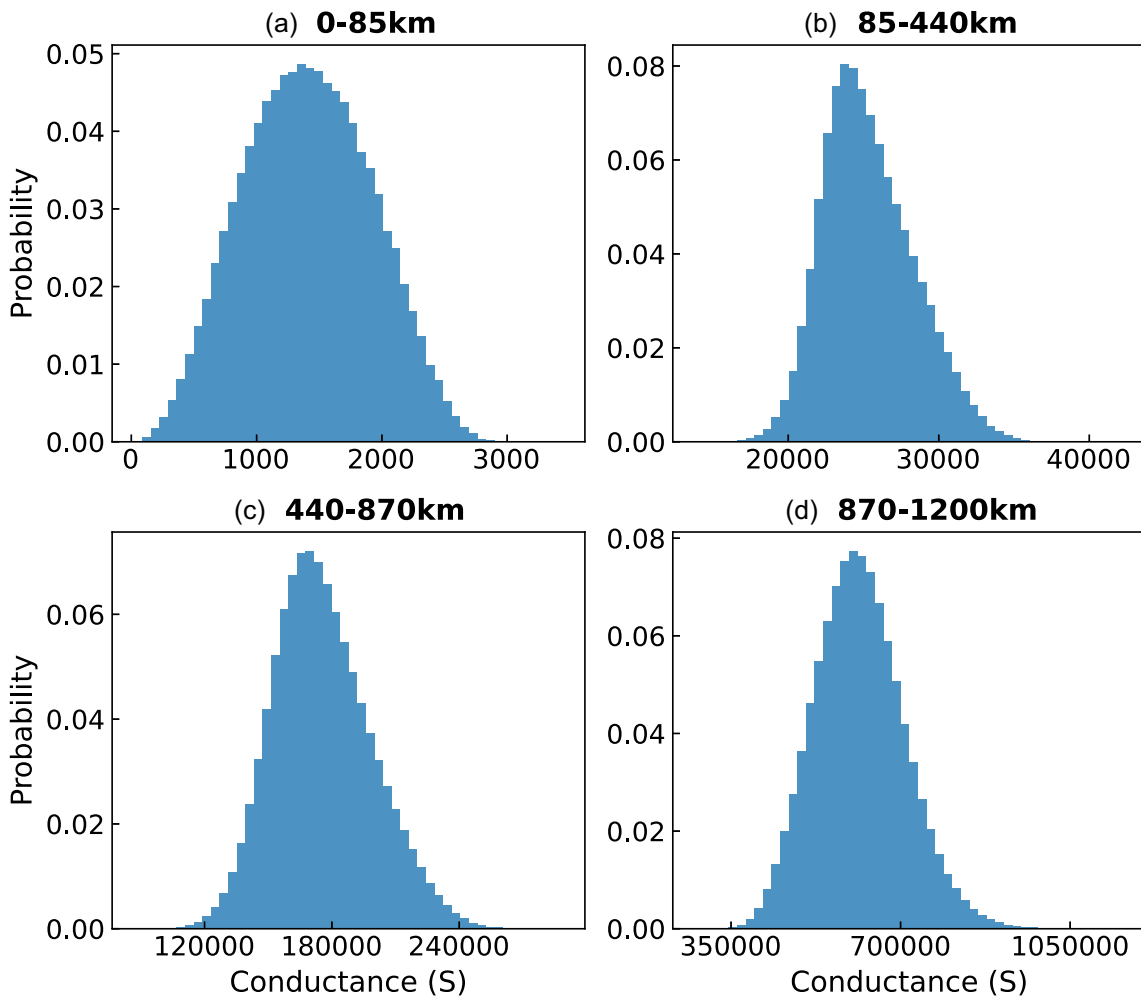


Figure 19. Histograms of the conductance (conductivity-thickness product) computed over different depth ranges for the joint posterior model distribution as shown in Fig. 17(c).

depths 51–104 km beneath western North America as the LAB. Lekić & Fischer (2014) detected a seismically defined LAB at 60–80 km depths beneath the western United States.

Mineral physics results suggest that there are conductivity jumps at major mineral phase transitions near the mantle transition zone (Yoshino & Katsura 2013). However, these discontinuities cannot be easily detected by the conventional regularized inversion without explicit constraints. Our Bayesian joint inverse model reveals a distinct conductivity jump at around 440 km. We test the sensitivity of data to this conductivity jump by forward modelling. Two modified models are tested. Compared to the original model, the modified model MTZ1 removes the conductivity jump at around 440 km, and the model MTZ2 reduces the conductivity jump in half.

Fig. 21 shows the original and modified conductivity models as well as the corresponding data fit. The data fit of the modified models changes distinctly for both MT and GDS responses, indicating that the transition zone conductivities are constrained simultaneously by two types of data. As presented in Table 2, the total RMS misfits increase by 204 per cent and 65 per cent for the modified models MTZ1 and MTZ2, implying the existence of the conductivity jump at around 440 km.

We also estimate the possible depth range of the ∼440 km layer interface. The RMS misfits for models that vary the ∼440 km conductivity jump to different depths are illustrated in Fig. 21(e). The result suggests that the mantle transition zone conductivity jump is located in the depth range of 440–460 km. This conductivity jump may be related to the global 410 km seismic discontinuity.

5 CONCLUSIONS

We have developed a new trans-dimensional Bayesian framework for the joint inversion of MT and GDS responses. This joint inversion framework has several features. First, it supports MT apparent resistivity and phase as well as various ionospheric and magnetospheric GDS responses. Secondly, a self-parametrizing trans-dimensional MCMC sampling algorithm was employed; it can automatically determine the number of layers. It can also quantitatively estimate the model uncertainty, which is crucial for reliable interpretations. Finally, the code was

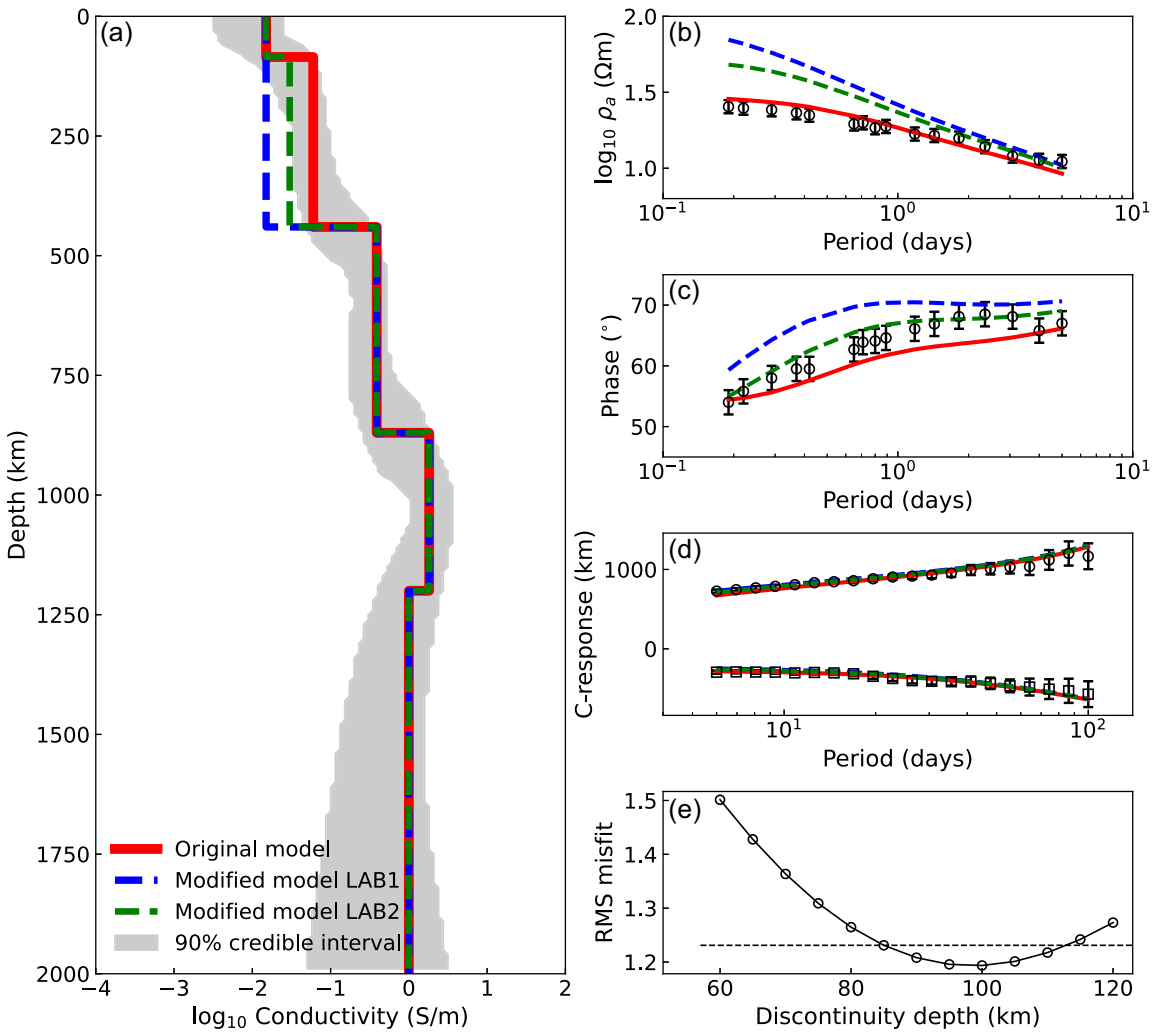


Figure 20. Sensitivity tests for the LAB. (a) The original and modified conductivity models and the corresponding (b) and (c) MT data fit and (d) GDS data fit. The corresponding changes in RMS misfit for the modified models are presented in Table 2. (e) RMS misfits for models that vary the ~85 km conductivity jump of the original model to different depths (solid line with circle symbols). The horizontal dash line denotes the RMS misfit of the original model.

Table 2. RMS data misfits for different modified 1D conductivity models used to discuss the main features of the inverse conductivity model beneath Tucson observatory.

Model	RMS misfit			Change in total RMS (per cent)
	MT data	GDS data	Total (MT+GDS)	
Original model	1.23	1.23	1.23	/
Modified model LAB1	4.39	1.38	3.55	188
Modified model LAB2	2.76	1.04	2.26	83
Modified model MTZ1	3.76	3.72	3.74	204
Modified model MTZ2	2.16	1.81	2.03	65

parallelized with MPI, so a large number of Markov chains can be run simultaneously to escape local minima and accelerate computations. To the best of our knowledge, this is the first implementation of the trans-dimensional Bayesian MCMC algorithm for the joint inversion of MT and GDS responses. We also released the inversion framework as an open-source C++ code, it would contribute to the imaging of deep mantle conductivities and the understanding of the composition, structures and dynamics of the Earth's interior. However, we should note that the MCMC algorithm still works only for 1D problem setups. For 3D problem setups, including, for example, proper treatment of the ocean induction effect (Chen *et al.* 2022), the MCMC algorithm is impracticable due to enormous computational costs.

We first applied the code to synthetic data sets. We demonstrated that compared to the separate inversion, joint inversion of MT and GDS responses obtained improved resolution and reduced uncertainty. To obtain reliable crustal and mantle conductivity structures, joint inversion

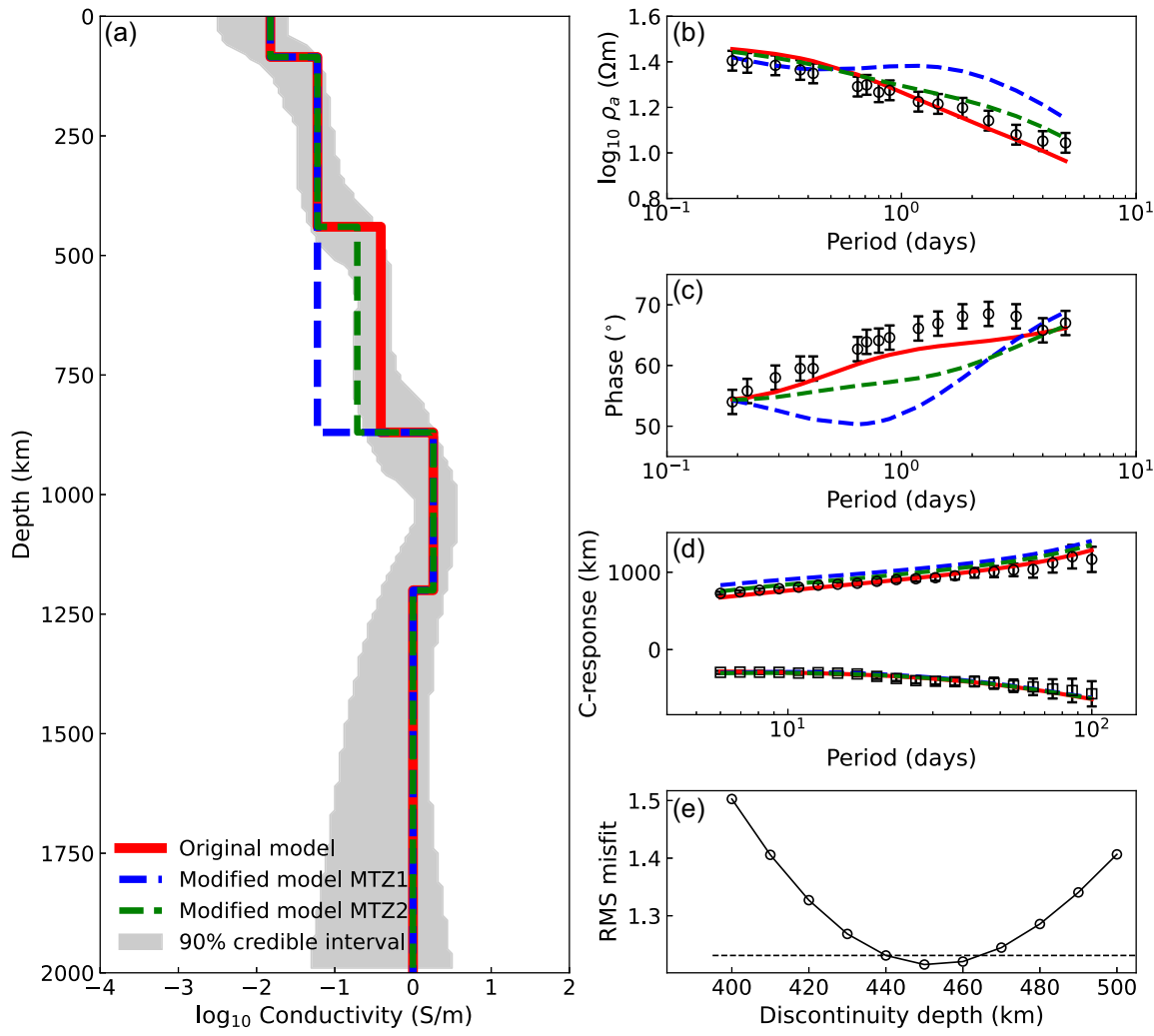


Figure 21. Similar to Fig. 20, but for the sensitivity tests of the ~ 440 km conductivity jump. The changes in RMS misfit for the modified models are presented in Table 2.

of MT and GDS responses is significant. We also showed that for both uniform and smooth priors of layer conductivities, the preset layer interfaces can be recovered by the joint inversion.

The developed trans-dimensional MCMC inversion code was then applied to the field MT and GDS responses at Tucson observatory, North America. We observed that running 48 chains simultaneously took only about 2 min for the joint inversion, illustrating the high efficiency of our implementation. The resulting Bayesian inverse models are in good agreement with the gradient-based L-BFGS inverse models, indicating that our new code can be well applied to field data. Combining uncertainty analysis and sensitivity tests, we summarize the following main features of the mantle conductivity model beneath Tucson: (1) Typical conductivities for depth intervals 0–85, 85–440, 440–870, and below 900 km are about 0.015, 0.06, 0.38, ad 1 S/m, respectively. (2) Distinct conductivity jumps are observed at around 85 and 440 km, which may be related to the LAB and the upper interface of the mantle transition zone, respectively.

DATA AND CODE AVAILABILITY

The Bayesian joint inversion code and the associated data are available at the GitHub repository (https://github.com/hongbo-yao/BayesMTG_DS-released).

ACKNOWLEDGMENTS

This work was financially supported by the National Natural Science Foundation of China (42250102, 41922027, 41830107, 42142034 and 42130810), the Open Fund from SinoProbe Laboratory (Sinoprobe Lab 202209), Innovation-Driven Project of Central South University (2020CX012), the Hunan Provincial Innovation Foundation for Postgraduate (CX20210277) and the Fundamental Research Funds for the

Central Universities of Central South University (2021zzts0259). We would like to thank the associated editor, Ute Weckmann, as well as the reviewer, Ronghua Peng, and an anonymous reviewer for their valuable comments and suggestions, which significantly improved the manuscript. We are grateful for resources from the High Performance Computing Center of Central South University.

REFERENCES

- Abt, D.L., Fischer, K.M., French, S.W., Ford, H.A., Yuan, H. & Romanowicz, B., 2010. North American lithospheric discontinuity structure imaged by Ps and Sp receiver functions, *J. geophys. Res.*, **115**, B09301.
- Agostinetti, N.P. & Malinverno, A., 2010. Receiver function inversion by trans-dimensional Monte Carlo sampling, *J. geophys. Int.*, **181**(2), 858–872.
- Alken, P. *et al.*, 2021. International geomagnetic reference field: the thirteenth generation, *Earth Planets Space*, **73**, 49.
- Aster, R.C., Borchers, B. & Thurber, C.H., 2018. *Parameter Estimation and Inverse Problems*, Elsevier.
- Bahr, K., Olsen, N. & Shankland, T.J., 1993. On the combination of the magnetotelluric and the geomagnetic depth sounding method for resolving an electrical conductivity increase at 400 km depth, *Geophys. Res. Lett.*, **20**(24), 2937–2940.
- Banks, R.J., 1969. Geomagnetic variations and the electrical conductivity of the upper mantle, *J. geophys. Int.*, **17**(5), 457–487.
- Blatter, D., Key, K., Ray, A., Foley, N., Tulaczyk, S. & Auken, E., 2018. Trans-dimensional Bayesian inversion of airborne transient EM data from Taylor Glacier, Antarctica, *J. geophys. Int.*, **214**(3), 1919–1936.
- Blatter, D., Key, K., Ray, A., Gustafson, C. & Evans, R., 2019. Bayesian joint inversion of controlled source electromagnetic and magnetotelluric data to image freshwater aquifer offshore New Jersey, *J. geophys. Int.*, **218**(3), 1822–1837.
- Bodin, T. & Sambridge, M., 2009. Seismic tomography with the reversible jump algorithm, *J. geophys. Int.*, **178**(3), 1411–1436.
- Bodin, T., Sambridge, M., Tkalcic, H., Arroucau, P., Gallagher, K. & Rawlinson, N., 2012. Transdimensional inversion of receiver functions and surface wave dispersion, *J. geophys. Res.: Solid Earth*, **117**(B2), B02301.
- Chave, A.D. & Jones, A.G., 2012. *The Magnetotelluric Method: Theory and Practice*, Cambridge University Press.
- Chave, A.D. & Thomson, D.J., 1989. Some comments on magnetotelluric response function estimation, *J. geophys. Res.: Solid Earth*, **94**(B10), 14215–14225.
- Chen, C., Kuvshinov, A., Kruglyakov, M., Munch, F. & Rigaud, R., 2022. Constraining the crustal and mantle conductivity structures beneath islands by a joint inversion of multi-source magnetic transfer functions, *J. Geophys. Res.: Solid Earth*, **128**(1), e2022JB024106.
- Civet, F., Thébault, E., Verhoeven, O., Langlais, B. & Saturnino, D., 2015. Electrical conductivity of the Earth's mantle from the first Swarm magnetic field measurements, *Geophys. Res. Lett.*, **42**(9), 3338–3346.
- Constable, S.C., Parker, R.L. & Constable, C.G., 1987. Occam's inversion: A practical algorithm for generating smooth models from electromagnetic sounding data, *Geophysics*, **52**(3), 289–300.
- Egbert, G.D. & Booker, J.R., 1992. Very long period magnetotellurics at Tucson Observatory: Implications for mantle conductivity, *J. geophys. Res.*, **97**(B11), 15099.
- Egbert, G.D., Booker, J.R. & Schultz, A., 1992. Very long period magnetotellurics at Tucson Observatory: Estimation of impedances, *J. geophys. Res.*, **97**(B11), 15113.
- Gehrman, R. A.S., Dettmer, J., Schwanenberg, K., Engels, M., Dosso, S.E. & Özmaral, A., 2015. Trans-dimensional Bayesian inversion of controlled-source electromagnetic data in the German North Sea, *Geophys. Prospect.*, **63**(6), 1314–1333.
- Geyer, C.J. & Möller, J., 1994. Simulation procedures and likelihood inference for spatial point processes, *Scandinavian J. Stat.*, **21**(4), 359–373.
- Grandis, H., Menivelle, M. & Roussignol, M., 1999. Bayesian inversion with Markov chains-I. The magnetotelluric one-dimensional case, *J. geophys. Int.*, **138**(3), 757–768.
- Grayver, A.V. & Kuvshinov, A.V., 2016. Exploring equivalence domain in nonlinear inverse problems using Covariance Matrix Adaption Evolution Strategy (CMAES) and random sampling, *J. geophys. Int.*, **205**(2), 971–987.
- Grayver, A.V., Munch, F.D., Kuvshinov, A.V., Khan, A., Sabaka, T.J. & Tøffner-Clausen, L., 2017. Joint inversion of satellite-detected tidal and magnetospheric signals constrains electrical conductivity and water content of the upper mantle and transition zone, *Geophys. Res. Lett.*, **44**(12), 6074–6081.
- Green, P.J., 1995. Reversible jump Markov Chain Monte Carlo computation and Bayesian model determination, *Biometrika*, **82**(4), 711–732.
- Guo, R., Dosso, S.E., Liu, J., Liu, Z. & Tong, X., 2014. Frequency- and spatial-correlated noise on layered magnetotelluric inversion, *J. geophys. Int.*, **199**(2), 1205–1213.
- Guo, R., Liu, L., Liu, J., Sun, Y. & Liu, R., 2019. Effect of data error correlations on trans-dimensional MT Bayesian inversions, *Earth Planets Space*, **71**, 134.
- Guzavina, M., Grayver, A. & Kuvshinov, A., 2019. Probing upper mantle electrical conductivity with daily magnetic variations using global-to-local transfer functions, *J. geophys. Int.*, **219**(3), 2125–2147.
- Hastings, W.K., 1970. Monte Carlo sampling methods using Markov chains and their applications, *Biometrika*, **57**(1), 97–109.
- Ichiki, M., Uyeshima, M., Utada, H., Guoze, Z., Ji, T. & Mingzhi, M., 2001. Upper mantle conductivity structure of the back-arc region beneath northeastern China, *Geophys. Res. Lett.*, **28**(19), 3773–3776.
- Kelbert, A., Egbert, G.D. & Schultz, A., 2008. Non-linear conjugate gradient inversion for global EM induction: resolution studies, *J. geophys. Int.*, **173**(2), 365–381.
- Kelbert, A., Schultz, A. & Egbert, G., 2009. Global electromagnetic induction constraints on transition-zone water content variations, *Nature*, **460**(7258), 1003–1006.
- Khan, A., Connolly, J. A.D. & Olsen, N., 2006. Constraining the composition and thermal state of the mantle beneath Europe from inversion of long-period electromagnetic sounding data, *J. geophys. Res.*, **111**, B10102.
- Khan, A., Kuvshinov, A. & Semenov, A., 2011. On the heterogeneous electrical conductivity structure of the Earth's mantle with implications for transition zone water content, *J. geophys. Res.*, **116**(B1), B01103.
- Kuvshinov, A. & Semenov, A., 2012. Global 3-D imaging of mantle electrical conductivity based on inversion of observatory C-responses-I. An approach and its verification, *J. geophys. Int.*, **189**(3), 1335–1352.
- Kuvshinov, A., Grayver, A., Tøffner-Clausen, L. & Olsen, N., 2021. Probing 3-D electrical conductivity of the mantle using 6 years of Swarm, CryoSat-2 and observatory magnetic data and exploiting matrix Q-responses approach, *Earth Planets Space*, **73**, 67.
- Kuvshinov, A.V., 2008. 3-D global induction in the oceans and solid earth: Recent progress in modeling magnetic and electric fields from sources of magnetospheric, ionospheric and oceanic origin, *Surveys geophys.*, **29**(2), 139–186.
- Lekić, V. & Fischer, K.M., 2014. Contrasting lithospheric signatures across the western United States revealed by Sp receiver functions, *Earth planet. Sci. Lett.*, **402**, 90–98.
- Li, X., Yuan, X. & Kind, R., 2007. The lithosphere-asthenosphere boundary beneath the western United States, *J. geophys. Int.*, **170**(2), 700–710.
- Lizarralde, D., Chave, A., Hirth, G. & Schultz, A., 1995. Northeastern Pacific mantle conductivity profile from long-period magnetotelluric sounding using Hawaii-to-California submarine cable data, *J. geophys. Res.: Solid Earth*, **100**(B9), 17837–17854.
- Macmillan, S. & Olsen, N., 2013. Observatory data and the Swarm mission, *Earth Planets Space*, **65**(11), 1355–1362.
- Malinverno, A., 2002. Parsimonious Bayesian Markov Chain Monte Carlo inversion in a nonlinear geophysical problem, *J. geophys. Int.*, **151**(3), 675–688.
- Mandolesi, E., Ogaya, X., Campanyà, J. & Agostinetti, N.P., 2018. A reversible-jump Markov Chain Monte Carlo algorithm for 1D inversion of magnetotelluric data, *Comput. Geosci.*, **113**, 94–105.

- Metropolis, N., Rosenbluth, A.W., Rosenbluth, M.N., Teller, A.H. & Teller, E., 1953. Equation of state calculations by fast computing machines, *J. Chem. Phys.*, **21**(6), 1087–1092.
- Minsley, B.J., 2011. A trans-dimensional Bayesian Markov Chain Monte Carlo algorithm for model assessment using frequency-domain electromagnetic data, *J. geophys. Int.*, **187**(1), 252–272.
- Minsley, B.J., Foks, N.L. & Bedrosian, P.A., 2021. Quantifying model structural uncertainty using airborne electromagnetic data, *J. geophys. Int.*, **224**(1), 590–607.
- Munch, F.D., Grayver, A.V., Kuvshinov, A. & Khan, A., 2018. Stochastic inversion of geomagnetic observatory data including rigorous treatment of the ocean induction effect with implications for transition zone water content and thermal structure, *J. geophys. Res.: Solid Earth*, **123**(1), 31–51.
- Munch, F.D., Grayver, A.V., Guzavina, M., Kuvshinov, A.V. & Khan, A., 2020. Joint inversion of daily and long-period geomagnetic transfer functions reveals lateral variations in mantle water content, *Geophys. Res. Lett.*, **47**(10), e2020GL087222.
- Olsen, N., 1999. Induction studies with satellite data, *Surveys geophys.*, **20**(3/4), 309–340.
- Peng, R., Yogeshwar, P., Liu, Y. & Hu, X., 2021. Transdimensional Markov Chain Monte Carlo joint inversion of direct current resistivity and transient electromagnetic data, *J. geophys. Int.*, **224**(2), 1429–1442.
- Peng, R., Han, B., Hu, X., Li, J. & Liu, Y., 2022. Transdimensional Bayesian inversion of magnetotelluric data in anisotropic layered media with galvanic distortion correction, *J. geophys. Int.*, **228**(3), 1494–1511.
- Püthe, C., Kuvshinov, A., Khan, A. & Olsen, N., 2015a. A new model of earth's radial conductivity structure derived from over 10 yr of satellite and observatory magnetic data, *J. geophys. Int.*, **203**(3), 1864–1872.
- Püthe, C., Kuvshinov, A. & Olsen, N., 2015b. Handling complex source structures in global EM induction studies: from C-responses to new arrays of transfer functions, *J. geophys. Int.*, **201**(1), 318–328.
- Ray, A. & Key, K., 2012. Bayesian inversion of marine CSEM data with a trans-dimensional self parametrizing algorithm, *J. geophys. Int.*, **191**(3), 1135–1151.
- Ren, Z. & Kalscheuer, T., 2020. Uncertainty and resolution analysis of 2D and 3D inversion models computed from geophysical electromagnetic data, *Surveys geophys.*, **41**(1), 47–112.
- Schmucker, U., 1999. A spherical harmonic analysis of solar daily variations in the years 1964–1965: response estimates and source fields for global induction-I. Methods, *J. geophys. Int.*, **136**(2), 439–454.
- Schultz, A., Kurtz, R.D., Chave, A.D. & Jones, A.G., 1993. Conductivity discontinuities in the upper mantle beneath a stable craton, *Geophys. Res. Lett.*, **20**(24), 2941–2944.
- Seillé, H. & Visser, G., 2020. Bayesian inversion of magnetotelluric data considering dimensionality discrepancies, *J. geophys. Int.*, **223**(3), 1565–1583.
- Semenov, A. & Kuvshinov, A., 2012. Global 3-D imaging of mantle conductivity based on inversion of observatory C-responses-II. Data analysis and results, *J. geophys. Int.*, **191**(3), 965–992.
- Shimizu, H., Koyama, T., Baba, K. & Utada, H., 2010. Revised 1-D mantle electrical conductivity structure beneath the north Pacific, *J. geophys. Int.*, **180**(3), 1030–1048.
- Utada, H., Koyama, T., Shimizu, H. & Chave, A.D., 2003. A semi-global reference model for electrical conductivity in the mid-mantle beneath the north Pacific region, *Geophys. Res. Lett.*, **30**(4), 1194.
- Verhoeven, O., Thébault, E., Saturnino, D., Houlié, A. & Langlais, B., 2021. Electrical conductivity and temperature of the Earth's mantle inferred from Bayesian inversion of Swarm vector magnetic data, *Phys. Earth planet. Inter.*, **314**, 106702.
- Ward, S.H. & Hohmann, G.W., 1987. Electromagnetic Theory for Geophysical Applications, in Nabighian, M.N., *Electromagnetic Methods in Applied Geophysics: Volume 1, Theory*, pp. Society of Exploration Geophysicists.131–311, ed.
- Xiang, E., Guo, R., Dosso, S.E., Liu, J., Dong, H. & Ren, Z., 2018. Efficient hierarchical trans-dimensional Bayesian inversion of magnetotelluric data, *J. geophys. Int.*, **213**(3), 1751–1767.
- Yao, H., Ren, Z., Tang, J. & Zhang, K., 2022. A multi-resolution finite-element approach for global electromagnetic induction modeling with application to southeast China coastal geomagnetic observatory studies, *J. geophys. Res.: Solid Earth*, **127**(8), e2022JB024659.
- Yin, C., Qi, Y., Liu, Y. & Cai, J., 2014. Trans-dimensional Bayesian inversion of frequency-domain airborne EM data, *Chinese J. Geophys. (in Chinese)*, **57**(9), 2971–2980.
- Yoshino, T. & Katsura, T., 2013. Electrical conductivity of mantle minerals: Role of water in conductivity anomalies, *Annual Rev. Earth planet. Sci.*, **41**(1), 605–628.
- Yuan, Y., Uyeshima, M., Huang, Q., Tang, J., Li, Q. & Teng, Y., 2020. Continental-scale deep electrical resistivity structure beneath China, *Tectonophysics*, **790**, 228559.
- Zhang, H., Egbert, G.D. & Huang, Q., 2022. A relatively dry mantle transition zone revealed by geomagnetic diurnal variations, *Sci. Advances*, **8**(31), eab03293.
- Zhang, Y., Weng, A., Li, S., Yang, Y., Tang, Y. & Liu, Y., 2020. Electrical conductivity in the mantle transition zone beneath Eastern China derived from L1-Norm C-responses, *J. geophys. Int.*, **221**(2), 1110–1124.